


Band Alignment in Monolayer Boron Phosphide with Janus MoSSe Heterobilayers under Strain and Electric Field

Y. Mogulkoc^{1,*}, R. Caglayan¹, and Y.O. Ciftci²

¹*Department of Physics Engineering, Faculty of Engineering, Ankara University, Tandogan, Ankara 06100, Turkey*

²*Department of Physics, Faculty of Sciences, Gazi University, Teknikokullar, Ankara 06500, Turkey*

 (Received 10 March 2021; revised 29 May 2021; accepted 24 June 2021; published 2 August 2021)

Recent studies have revealed that Janus structures and heterobilayers made from them might have properties superior to those of two-dimensional (2D) materials. We construct 2D monolayer boron phosphide (MBP)/MoSSe and MoSSe/MBP heterobilayers and describe comprehensively their optoelectronic properties in the presence of biaxial in-plane and uniaxial out-of-plane strain and the effects of electric fields using first-principles methods. The electronic bands of both MBP/MoSSe and MoSSe/MBP heterobilayers display a peculiarity in the direct gap, with different band-gap values in the pristine forms. Remarkably, it is shown that different varieties of band alignments are induced for different orders of the van der Waals (vdW) heterobilayers. Electric fields and in-plane and out-of-plane strain give rise to important changes in the electronic and optical properties. The band alignments can transform from type I to type II under the influence of an electric field and strain. The main absorption peaks of pristine forms of both heterobilayers have in the visible region (approximately 2.67 eV), while in the presence of biaxial strain are redshifted. Since the absorption peaks of the pristine forms of the heterobilayers are in the visible region, the heterobilayers recommended here can be used in photovoltaic applications, and the presence of effects of external electric fields and strain promises functional optoelectronic devices.

DOI: [10.1103/PhysRevApplied.16.024001](https://doi.org/10.1103/PhysRevApplied.16.024001)

I. INTRODUCTION

Two-dimensional (2D) materials are of extensive interest due to their extraordinary optoelectronic properties when used in electronic devices [1–8]. Graphene [9], which pioneered 2D materials, has had limited electronic applications due to its zero band gap. Therefore, 2D materials such as transition-metal dichalcogenides (TMDCs) [4,8,10–12], phosphorene [13–17], and lateral heterostructures [18] have been extensively studied. For instance, the band gaps of TMDCs are adjustable in the 1–3-eV range, providing flexibility in optoelectronic applications. In addition, 2D van der Waals (vdW) heterobilayers [19] based on these 2D materials have also been studied both theoretically and experimentally. These vdW heterobilayers are obtained by vertically stacking two distinct 2D materials via the vdW interaction, and they exhibit diverse functional properties compared with their constituent monolayers; e.g., 2D phosphorene/SnS₂ (SnSe₂) heterobilayers can be used in tunnel field-effect transistors [20]. Furthermore, hexagonal boron nitride (*h*-BN), a group III-V compound, is an insulator that has a band gap around 6 eV with high thermal and chemical stability

[21–27]. Monolayer boron phosphide (MBP), with a carrier mobility of over $10^4 \text{ cm}^2 \text{ V}^{-1} \text{ s}^{-1}$ [28–30], has a direct band gap and can be used in nanoscale semiconductors for electronic devices [25,31–35]. In addition, MBP can be synthesized on silicon carbide (SiC) substrates using the chemical vapor deposition (CVD) method [36].

Moreover, MoS₂ has been demonstrated as another practicable material for applications in optoelectronic devices due to its moderate band gap (approximately 1.57 eV) [4,5,8,37]. Its electronic structure is dependent on the strain in the layers and the carrier mobility [38,39]. Changing the planar symmetry of TMDCs is an effective approach to obtaining better physical and chemical properties for use in transistor and sensor devices made from 2D materials, for example by constructing Janus *MX**Y* structures [40,41]. The Janus MoSSe structure is constructed by breaking the out-of-plane symmetry of the MoS₂ monolayer and replacing a S atom with a Se atom. Thus, breaking the out-of-plane symmetry results in an intrinsic electric field. When two-dimensional Janus materials are synthesized, theoretical and experimental applications are envisioned in different fields. Very recently, Janus MoSSe has been fabricated on sapphire substrates by using the CVD method [42]. Janus *MX**Y* structures have different features compared with *MX*₂ structures. For example,

*mogulkoc@eng.ankara.edu.tr

TABLE I. Lattice constant (a_0), interlayer distance (Δ), binding energy (E_b), and electronic band gap (E).

	a_0 (Å)	Δ (Å)	E_b (eV)	E^{PBE} (eV)	E^{HSE06} (eV)
MBP	3.212	—	—	0.907	1.362
MoSSe	3.249	—	—	1.558	2.018
MBP/MoSSe	3.227	3.196	-1.033	0.814	1.271
MoSSe/MBP	3.228	3.432	-1.028	0.949	1.322

a MoSSe monolayer can be used for photocatalytic water splitting as a consequence of the intrinsic electric field [43–46]. However, similarly to MoS₂ and MoSe₂, the low electron mobility (approximately 50 cm² V⁻¹ s⁻¹) [45], high recombination rate, and short lifetime of photo-generated electron-hole pairs limit the practical electronic applications of MoSSe monolayers. Peng and coworkers [47] have proposed that doping Cr or V into Janus MoSSe can induce valley polarization, which allows valleytronics applications. WSeTe monolayers can be used in applications of out-of-plane piezoelectricity and in spintronics applications due to Rashba splitting induced by the effect of spin-orbit coupling. Zhang *et al.* [48] proposed that Janus VSSe monolayers have potential applications in nanoelectronics, optoelectronics, and valleytronics due to combining ferromagnetism, ferroelasticity, piezoelectricity, and valley polarization. In the literature, there are many studies of different vdW 2D heterobilayers [49–55]. It is important to consider the band alignments to specify the fields of application of vdW heterobilayers [56]. In general, vdW heterobilayers present three different band alignments, which are type I (straddling), type II (staggered), and type III (broken-gap). Type-I heterobilayers are used in optoelectronic devices such as light-emitting diodes [57–61] and quantum-well lasers [62,63] as a

TABLE II. Binding energies of MBP (MoSSe)/MoSSe (MBP) heterobilayers for the AA1, AA2, AB1, AB2, AB3, and AB4 stacking patterns.

	MBP/MoSSe (eV)	MoSSe/MBP (eV)
AA1	-0.9741	-0.9968
AA2	-1.0332	-1.0277
AB1	-0.9456	-0.9604
AB2	-0.9539	-0.9706
AB3	-1.0008	-1.0002
AB4	-0.9606	-0.9769

consequence of efficient electron-hole recombination due to the spatial confinement of electrons and holes. In type-II heterobilayers, the undesired recombination rate of photo-generated carriers [64] is reduced due to spatial separation of the electron-hole pairs. Besides, type-II alignment plays an important role in photovoltaic [65–67] and photocatalytic [68–70] applications, as it modulates the properties of the constituent 2D materials. Type-III band alignment is used in tunnel field-effect transistors [71] and wavelength photodetectors [72], since it facilitates transitions from the conduction to the valence band. Thus, a stronger energy transition enhances the magnetic proximity effect and thereby intensifies the valley splitting [73]. Shang *et al.* [74] stated that bilayer MoSSe has a type-II band alignment due to an intrinsic dipole, which makes it a good candidate for optoelectronic applications. In a study of a blue phosphorus/MoSSe [49] vdW heterobilayer, it was shown that the electronic band structure could be modulated by an external electric field and in-plane strain. In addition, it was shown that type-I and type-II band alignments were obtained by the replacement of S and Se atoms, respectively, in the MoSSe structure. The variation of the electronic and optical properties of different types of

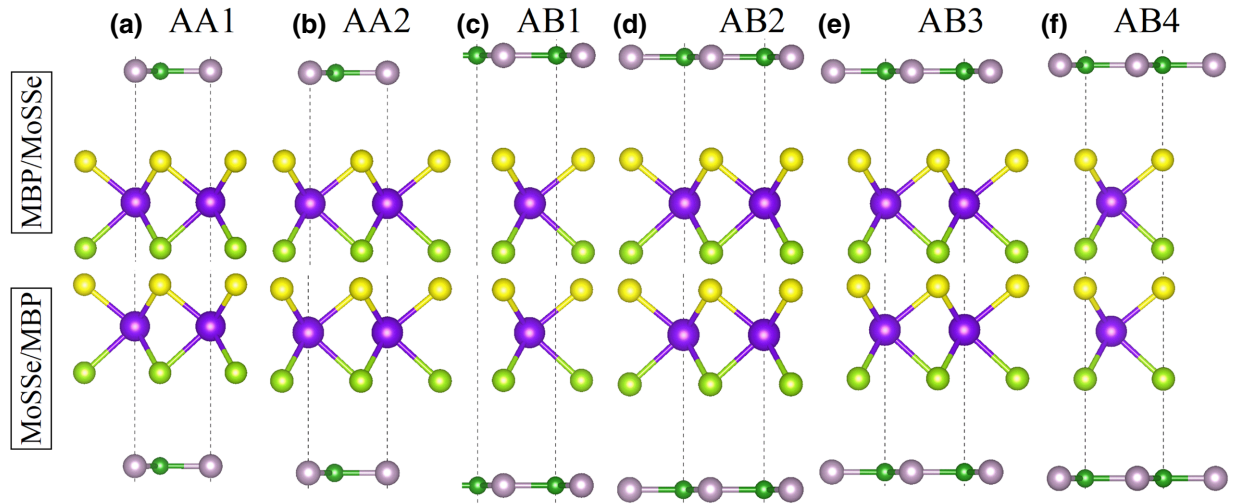


FIG. 1. Stacking patterns considered for the MBP (MoSSe)/MoSSe (MBP) heterostructures.

similar heterobilayers under electric fields and strain was studied by Mogulkoc *et al.* [28,41], Jappor *et al.* [75], and Caglayan *et al.* [76].

In this paper, the optoelectronic properties of MBP/MoSSe and MoSSe/MBP vdW heterobilayers under external influences such as electric fields, biaxial in-plane strains, and uniaxial out-of-plane strains are comprehensively investigated by first-principles methods. Six possible stacking patterns are considered for both heterobilayers. All stacking patterns are examined both energetically and dynamically to determine the most favorable pattern. Subsequently, to identify the band alignments, the electronic band structures and interlayer charge transfers in pristine heterobilayers are examined. The variation of the band alignment in the heterobilayers under the influence of an external electric field and in-plane and out-of-plane strain is studied. Finally, since these MBP/MoSSe and MoSSe/MBP heterobilayers have not yet been synthesized, some experimental steps to achieve this are proposed in the Appendix.

II. METHOD

First-principles calculations based on density-functional theory are performed using the projected-augmented-wave method [77] implemented in the Vienna *ab initio* simulation package (VASP) [78–81]. The exchange-correlation

functional is approximated by the generalized gradient approximation formulated by Perdew, Burke, and Ernzerhof (PBE) [82]. The conjugate gradient method is used to optimize atomic positions and lattice constant. The cutoff energy of the plane wave is set to 700 eV. The Brillouin-zone integration is performed using the gamma-centered Monkhorst-Pack method [83] with $16 \times 16 \times 1$ k -points. The DFT-D2 method [84] proposed by Grimme is employed to describe the effect of vdW interactions between the MBP and MoSSe. In the geometrical optimization, the maximum Hellmann-Feynman force acting on each atom is less than 0.05 eV/Å. The convergence criterion for the energy between consecutive steps is taken to be 10^{-6} eV. The vacuum layer along the z direction to prevent interactions between neighboring slabs is 20 Å thick. The Heyd-Scuseria-Ernzerhof (HSE06) [85,86] screened hybrid functional is applied to correct the underestimated band-gap values. The Bader charge analysis developed by Tang *et al.* [87], Sanville *et al.* [88], and Henkelman *et al.* [89] is performed to investigate the charge transfer between the two layers. The phonon frequencies are calculated using the PHONOPY [90] code based on density-functional perturbation theory. All phonon calculations are done employing a $3 \times 3 \times 1$ supercell approximation.

Finally, the dielectric functions of the heterobilayers are calculated by using the random-phase approximation [91]

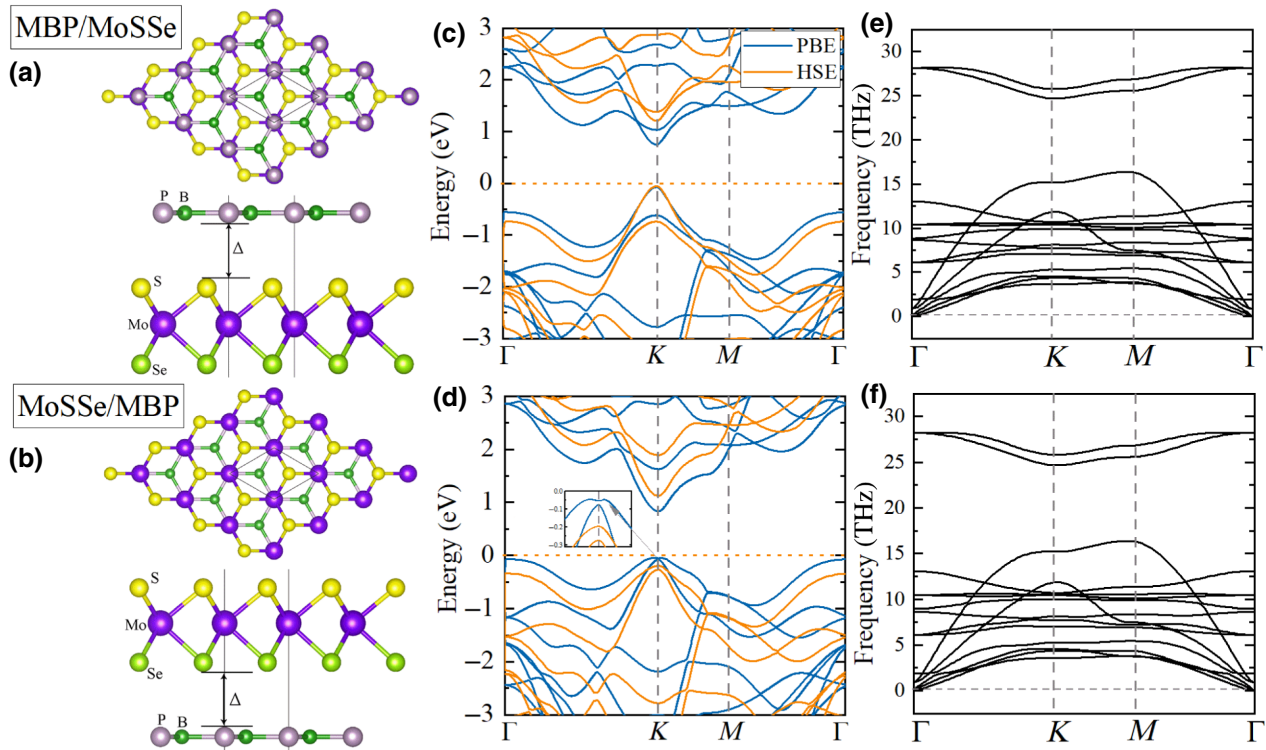


FIG. 2. (a),(b) Top and side views of stable atomic configurations, (c),(d) electronic band structures, and (e),(f) phonon dispersion curves for the optimized MBP/MoSSe and MoSSe/MBP heterobilayers.

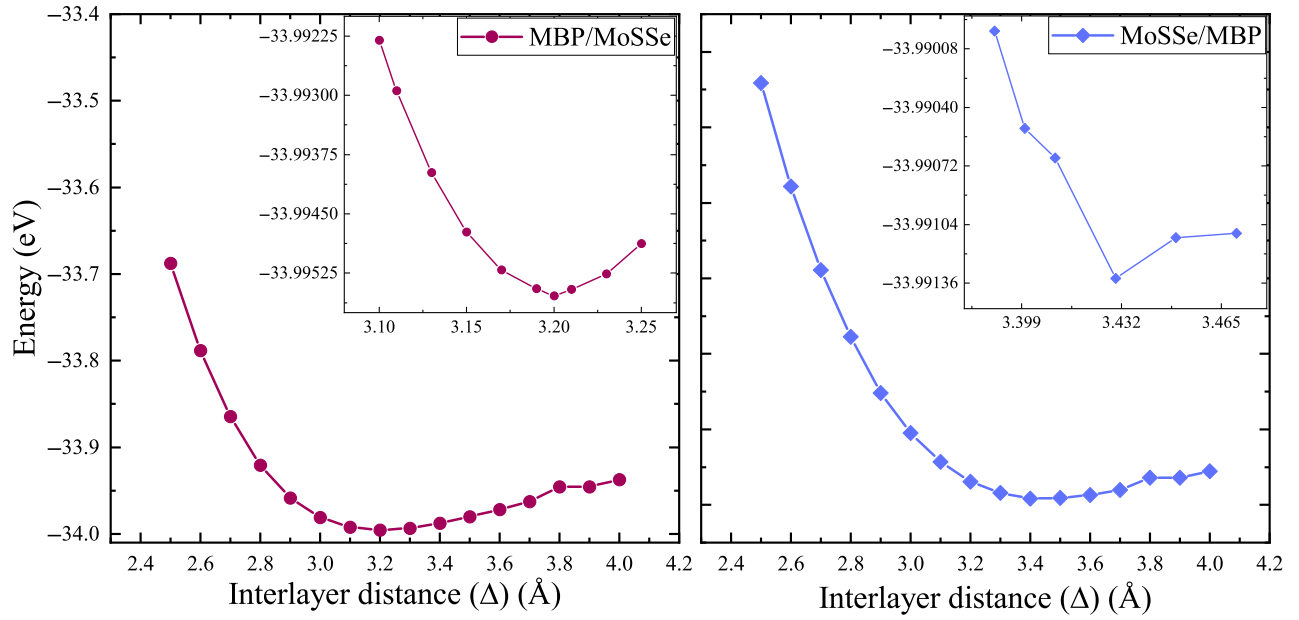


FIG. 3. Variation of total energy of MBP (MoSSe)/MoSSe (MBP) heterobilayers as a function of interlayer distance.

on top of the PBE functional with local field effects for sampling at $57 \times 57 \times 1$ k -points. The linear response of a system due to external electromagnetic radiation is defined by the complex dielectric function $\epsilon(\omega) = \epsilon_1(\omega) + i\epsilon_2(\omega)$. The imaginary part $\epsilon_2(\omega)$ of the dielectric function due to direct interband transitions is given by an expression derived from the momentum matrix elements between the occupied and unoccupied wave functions as follows [92]:

$$\epsilon_{\alpha\beta}^2(\omega) = \frac{4\pi^2 e^2}{\Omega} \lim_{q \rightarrow 0} \frac{1}{q^2} \sum_{c,v,\mathbf{k}} 2\omega_{\mathbf{k}} \delta(\epsilon_{c\mathbf{k}} - \epsilon_{v\mathbf{k}} - \omega) \times \langle u_{c+\mathbf{k}+\mathbf{e}_{\alpha q}} | u_{v\mathbf{k}} \rangle \langle u_{c+\mathbf{k}+\mathbf{e}_{\beta q}} | u_{v\mathbf{k}} \rangle^*,$$

where c and v correspond to conduction- and valence-band states, respectively, and $u_{c\mathbf{k}}$ is the cell-periodic part of the orbitals at the k -point \mathbf{k} .

III. RESULTS AND DISCUSSION

A. Structural and electronic properties

We examine the structural parameters of pristine MBP and Janus MoSSe before investigating the MBP (MoSSe)/MoSSe (MBP) heterobilayers. As can be seen from Table I, the calculated lattice parameters of MBP and MoSSe are 3.212 [28,93] and 3.249 Å [43,52], respectively, which are compatible with previous reports. Stacking two different monolayers can present a significant challenge because of the lattice mismatch, which can cause

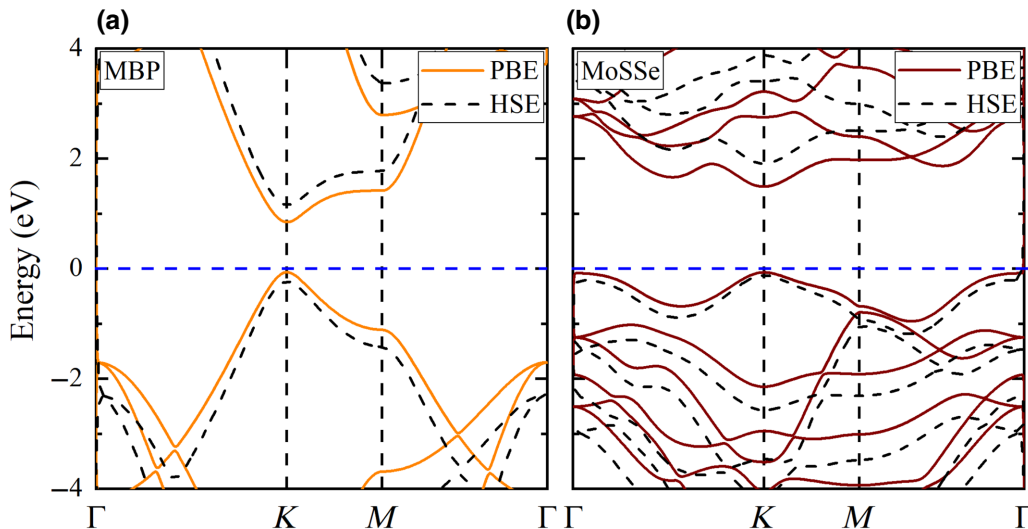


FIG. 4. Electronic band structures of (a) pristine MBP and (b) Janus MoSSe from PBE method (solid lines) and HSE06 method (dashed lines).

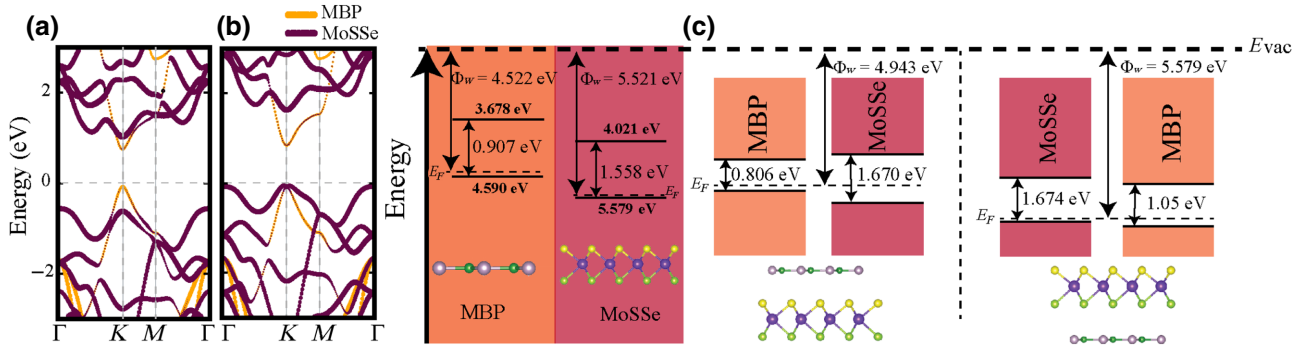


FIG. 5. Layer-dependent projected electronic band structures for (a) MBP/MoSSe and (b) MoSSe/MBP heterobilayers. (c) Schematic representation of band alignments of heterobilayers. E_F and E_{vac} represent the Fermi and vacuum energies, respectively.

a strain effect in the unit cell. Besides, the lattice mismatch creates alterations in the optoelectronic properties and may even influence the dynamical stability of the heterobilayer. In the condition where MBP (MoSSe) and MoSSe (MBP) are stacked, this results in a rather small lattice mismatch of around 1.13%. Because of the broken out-of-plane symmetry of MoSSe, two distinct types of heterobilayer, formed by placing the MBP above and below the MoSSe, are considered. Also, six possible stacking patterns, called AA1, AA2, AB1, AB2, AB3, and AB4, are considered for each heterobilayer (see Fig. 1). A convenient stacking pattern is found with the binding energy expressed by $E_b = E_{MBP(MoSSe)/MoSSe(MBP)} - E_{MBP} - E_{MoSSe}$, where

$E_{MBP(MoSSe)/MoSSe(MBP)}$, E_{MBP} , and E_{MoSSe} stand for the total energies of the heterobilayers (see Table II). Illustrations of both of the stable heterobilayers are given in Figs. 2(a) and 2(b). The lattice parameters of the MBP/MoSSe and MoSSe/MBP heterobilayers are found to be 3.227 and 3.228 Å, respectively, as can also be seen in Table I. The binding energies of both heterobilayers are around -1 eV. Hence, it can be assumed that there is energetically favorable and relatively strong vdW bonding between the MBP and MoSSe. Also, the interlayer distances (Δ) of both heterobilayers are investigated from 2.5 to 4 Å (see Fig. 3) and are found to be about 3 Å, which is a typical equilibrium distance for vdW heterobilayers [76].

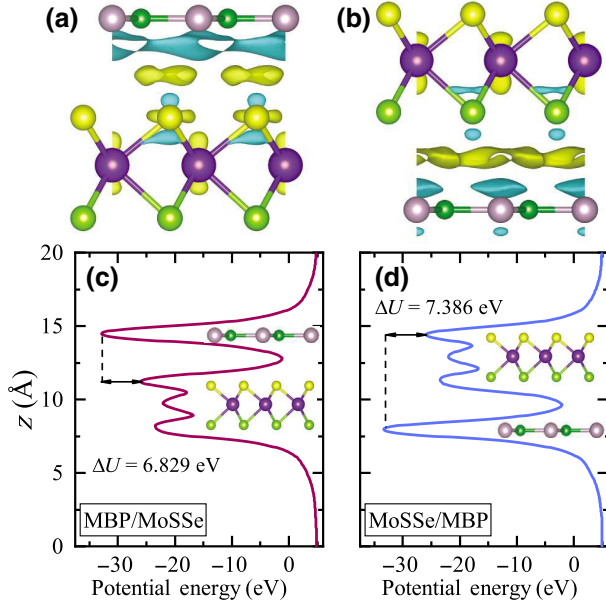


FIG. 6. (a),(b) Band-decomposed charge-density differences and (c),(d) in-plane average electrostatic potential in MBP (MoSSe)/MoSSe (MBP) heterobilayers. The blue and yellow colors represent charge-depletion and accumulation regions, respectively. The isosurface value is set to $0.0002 e \text{ \AA}^{-3}$.

The dynamical stability of the heterobilayers is examined by use of phonon spectra. Both heterobilayers are vibrationally stable with optimized lattice parameters due to their positive phonon branches, as depicted in Figs. 2(e) and 2(f). The electronic band structures of pristine MBP and MoSSe are presented in Fig. 4. MBP and MoSSe are direct semiconductors, with band-gap values of 0.907 (1.362) and 1.558 eV (2.018 eV), respectively, for the PBE (HSE06) method. The conduction-band minimum (CBM) and valence-band maximum (VBM) are at the K point in the Brillouin zone. As pointed out in Figs. 2(c) and 2(d), the electronic band structure of the MBP/MoSSe heterobilayer has a direct semiconducting behavior for both the PBE and the HSE06 methods. As expected, the HSE06 method increases the band gap by lifting the CBM without changing the trend of the band structure. However, the MoSSe/MBP heterobilayer exhibits indirect semiconducting behavior for the PBE method only. In addition, the MoSSe/MBP

TABLE III. Bader charge analysis and dipole moment (μ).

	MBP ($ e $)	MoSSe ($ e $)	μ ($e \text{ \AA}$)
MBP/MoSSe	0.018	-0.018	0.027
MoSSe/MBP	0.011	-0.011	0.041

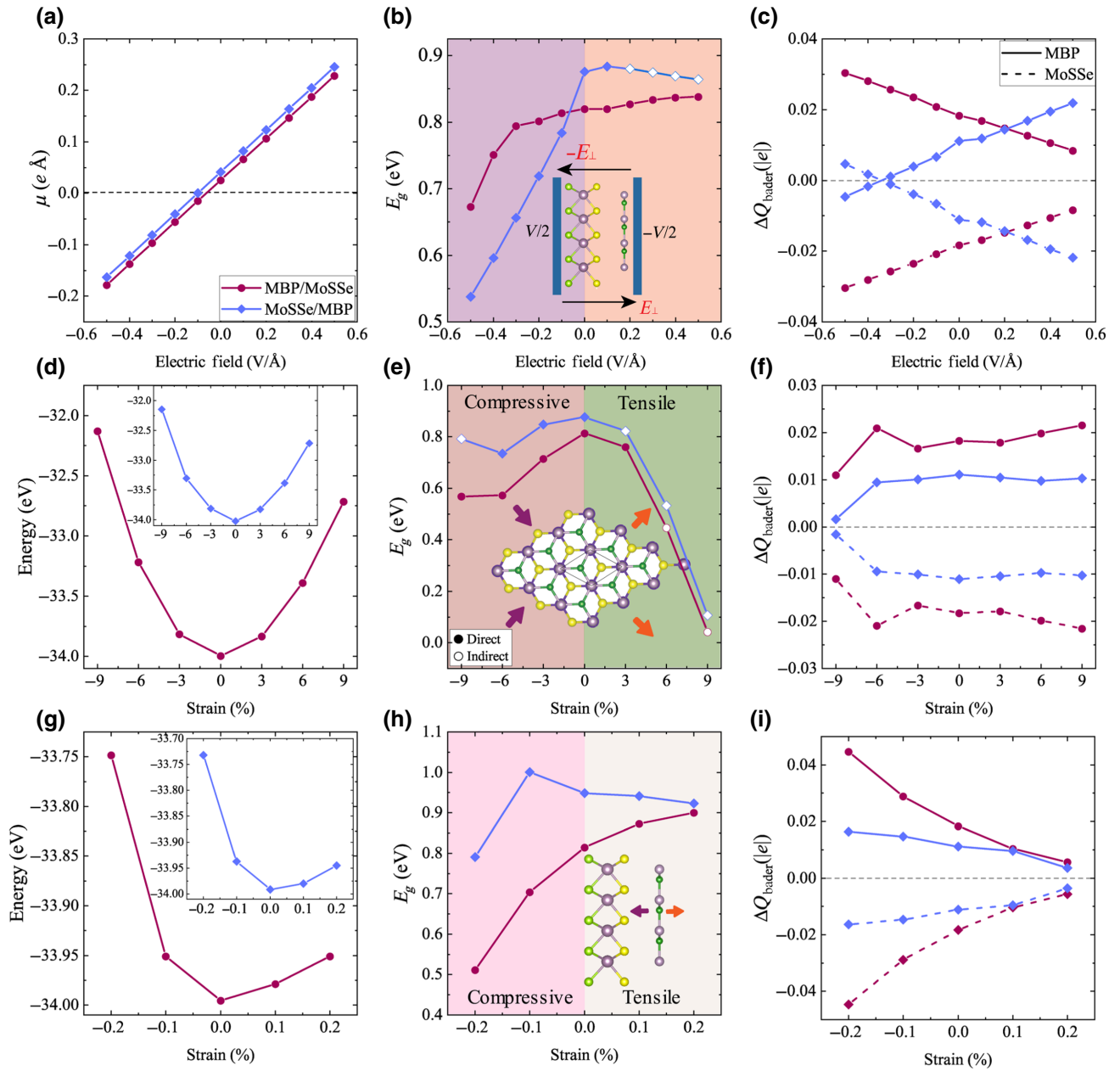


FIG. 7. Variation of (a) dipole moment, (b) electronic band gap, and (c) interlayer charge transfer in the presence of an external electric field. Variation of (d) total energy, (e) electronic band gap, and (f) interlayer charge transfer as a function of biaxial strain in MBP (MoSSe)/MoSSe (MBP) heterobilayers. Variation of (g) total energy, (h) electronic band gap, and (i) interlayer charge transfer as a function of out-of-plane strain in MBP (MoSSe)/MoSSe (MBP) heterobilayers.

heterobilayer has a Mexican-hat-like valence-band structure due to the band degeneracy at the VBM. For the HSE06 method, the band gap increases, with shifting both of the CBM upward and of the VBM downward. Thus the degeneracy in the VBM is split.

The layer-dependent projected electronic band structures and corresponding band alignments of the MBP/MoSSe and MoSSe/MBP heterobilayers are presented in Fig. 5. As can be seen from Figs. 5(a) and 5(b), for the MBP/MoSSe heterobilayer, the contributions to the CBM

and VBM originate from the MBP layer. When the layer order of the two-dimensional structure is changed, i.e., a MoSSe/MBP heterobilayer is formed, the VBM has contributions from both the MoSSe and the MBP, but the MoSSe layer is dominant. Also, the band edges of all structures belonging to the heterobilayers are presented in Fig. 5(c), where the band alignments are set to the energy of a stable electron within the vacuum level. The work function of the structures is considered by use of the formula $\Phi_w = E_{\text{vac}} - E_F$. Here, E_{vac} and E_F denote

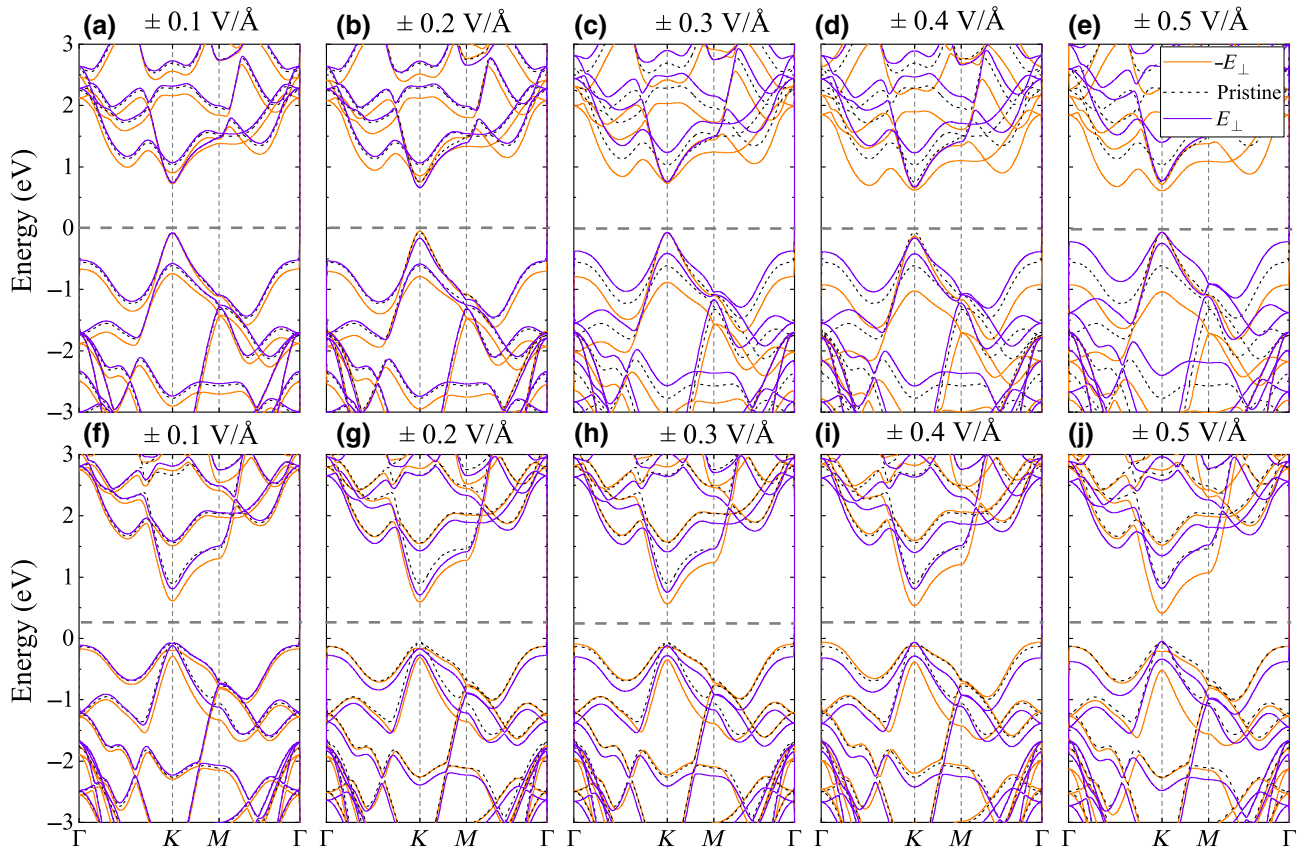


FIG. 8. Energy-band spectra of (a)–(e) MBP/MoSSe and (f)–(j) MoSSe/MBP heterobilayers under the influence of a perpendicular electric field.

the vacuum and Fermi energies, respectively. The work functions of freestanding monolayer boron phosphide and monolayer Janus MoSSe are found to be 4.522 and 5.521 eV, respectively, which are comparable with reported values for monolayer boron phosphide (4.66 eV) [28] and MoSSe (5.24 eV) [94]. The band alignments of vdW heterobilayers are determined by the contributions of the layers to the conduction and valence bands. In this case, for the MBP/MoSSe heterobilayer, the contributions to the conduction and valence bands are provided by the monolayer boron phosphide, which leads to a type-I band alignment at the interface. On the other hand, for the MoSSe/MBP heterobilayer, the contributions to the conduction and valence bands are provided by the monolayer boron phosphide and the MoSSe, respectively, which leads to a type-II band alignment at the interface of the heterobilayer. These results are consistent with the previous studies of MX_2 /MBP ($M = \text{Mo}, \text{W}; X = \text{S}, \text{Se}$) heterobilayers [56,93].

The charge-density differences of the heterobilayers are presented in Figs. 6(a) and 6(b). The band-decomposed charge density refers to the valence-band maximum and the conduction-band minimum in the band structure, as shown in Figs. 5(a) and 5(b). Figure 6(a) shows that the VBM is mainly located at the sulfur atoms for the

MBP/MoSSe heterobilayer and refers to the free electron pairs at boron atoms. Figure 5(b) exhibits the VBMs at the K point for the band structures of both MBP and MoSSe, which are consistent with the decomposed charge density in Fig. 6(b). Also, the amount of charge transfer between the interlayers of monolayers in each heterobilayer is given in Table III. It is clear that charge is transferred from the MBP to the MoSSe layer and a higher charge transfer occurs in the MBP/MoSSe heterobilayer, which is compatible with the lower interlayer distance and lower binding energy. Furthermore, we examine the electrostatic potentials, as shown in Figs. 6(c) and 6(d). MBP has a deeper potential than MoSSe, from which it can be concluded that charge is transferred from MBP to MoSSe. This result is also consistent with the Bader charge analysis. As mentioned, MoSSe has an intrinsic electric field, which results from a broken out-of-plane symmetry. This broken symmetry constitutes an intrinsic dipole in monolayer MoSSe. Accordingly, the out-of-plane dipole moment of pristine MoSSe is found to be 0.181 debye, which is compatible with previous reports [74,95]. In addition, an intrinsic dipole exists in the interlayer of a vdW heterobilayer, which creates an intrinsic electric field. For this situation, the dipole moment of MBP (MoSSe)/MoSSe (MBP) is found to be 0.027 (0.041) eÅ (0.123 (0.197) Debye),

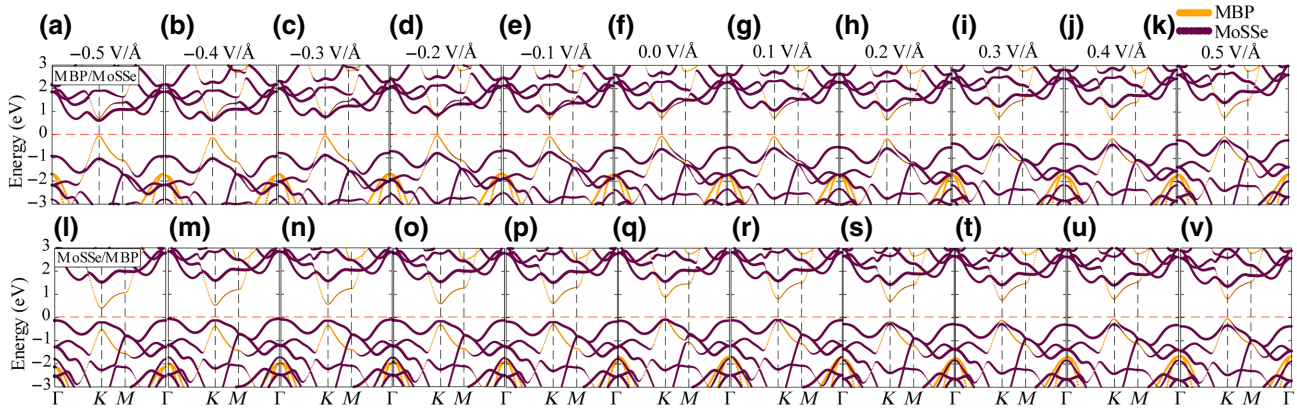


FIG. 9. Layer-dependent electronic band structures of (a)–(k) MBP/MoSSe and (l)–(v) MoSSe/MBP in the presence of an external perpendicular electric field.

as also stated in Table III. The electrostatic potential difference between the two constituent monolayers of the MBP/MoSSe and MoSSe/MBP heterobilayers is approximately 6.8 and 7.3 eV, respectively. Consequently, a large electrostatic potential difference imposes a strong electric field across the interfacial region of the heterobilayers.

In general, applying external electric fields and strains to vdW heterobilayers plays an effective role in modulating the electronic properties and thereby diversifying the application range. Thus, we examine the effects of an external perpendicular electric field and biaxial strain on the MBP (MoSSe)/MoSSe (MBP) heterobilayers. As presented in the inset of Fig. 7(b), the electric field is applied perpendicular to the surface of the heterobilayer and is directed from the MBP (MoSSe) to the MoSSe (MBP) for the MoSSe (MBP)/MBP (MoSSe) heterobilayers. The

electronic band structures and the band-gap variations for both heterobilayers under the influence of the external electric field are presented in Figs. 7(b) and 8, respectively. As indicated in Fig. 7(b), the band gap of the MBP/MoSSe heterobilayer increases between -0.5 V \AA^{-1} (0.673 eV) and 0.5 V \AA^{-1} (0.838 eV) with preservation of the direct-band-gap feature. For the MoSSe/MBP heterobilayer, with the transition from a direct to an indirect gap, the band gap increases linearly between -0.5 V \AA^{-1} (0.538 eV) and 0.1 V \AA^{-1} (0.883 eV) and decreases indistinctly between 0.2 V \AA^{-1} (0.880 eV) and 0.5 V \AA^{-1} (0.865 eV). The evolution of the dipole moments with respect to the applied electric field is presented in Fig. 7(a). The variation of the dipole moments of both heterobilayers depends on the direction and magnitude of the electric field. The intrinsic electric

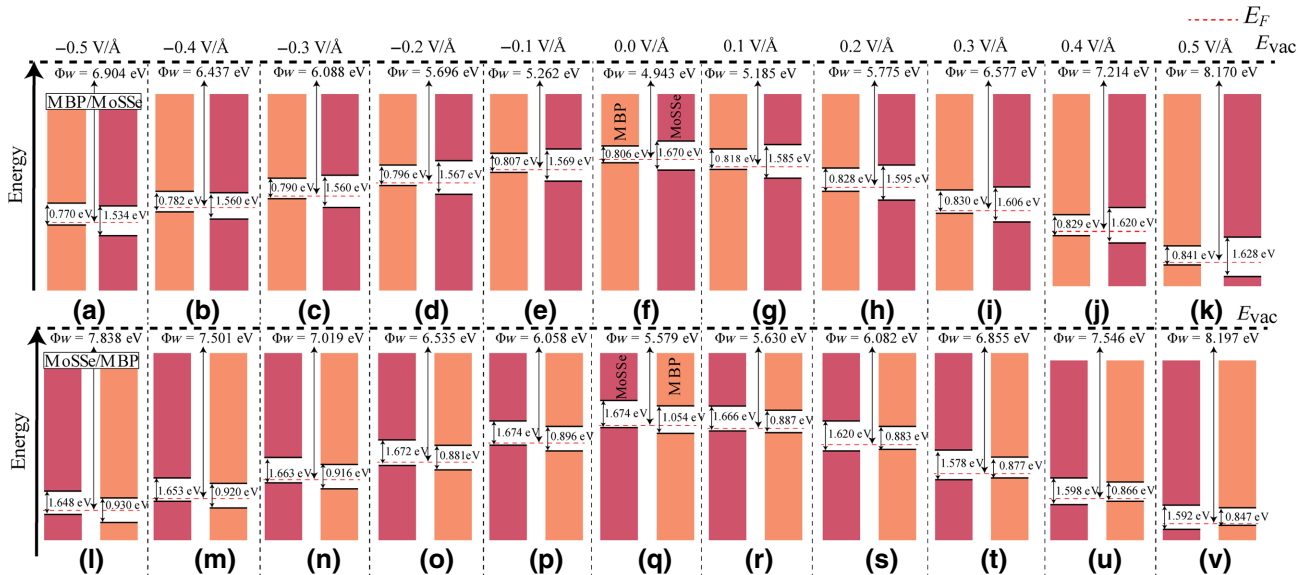


FIG. 10. Variation of the band alignments of (a)–(k) MBP/MoSSe and (l)–(v) MoSSe/MBP in the presence of an external electric field.

field is directed from the S atoms to the MBP for the MBP/MoSSe heterobilayer. Nonetheless, an applied electric field in the positive direction strengthens the intrinsic electric field and decreases the charge transfer between the MBP and MoSSe layers. Hence, the band gap is enhanced with decreasing charge transfer. On the other hand, for the negative direction of the external electric field applied to the MBP/MoSSe heterobilayer, the directions of the intrinsic electric field and the external perpendicular electric field differ from each other. Because of this, these two electric fields compensate each other and increase the charge transfer [see Fig. 7(c)], and correspondingly the band gap decreases. In the MoSSe/MBP heterobilayer, similarly to the MBP/MoSSe heterobilayer, the intrinsic electric field is directed from the Se atoms to the MBP layer, i.e., from the MoSSe layer to the MBP layer. When the external electric field is in the positive direction and the intrinsic electric field is in the opposite direction, these two fields quench each other. Therefore, as presented in Fig. 7(c), as the magnitude of the electric field increases in the positive region, the charge transfer between the layers increases, and consequently the band gap decreases. Interestingly, in the MoSSe/MBP heterobilayer, with an increasing magnitude of the external electric field in the negative region, the band gap decreases, and a direct-indirect band-gap transition occurs. This can be explained by the variations of the dipole moments of

TABLE IV. Variation of band alignments in the presence of an external electric field.

Electric field (V \AA^{-1})	MBP/MoSSe	MoSSe/MBP
-0.5	Type II	Type II
-0.4	Type II	Type II
-0.3	Type I	Type II
-0.2	Type I	Type II
-0.1	Type I	Type II
0.0	Type I	Type II
0.1	Type I	Type II
0.2	Type I	Type I
0.3	Type I	Type I
0.4	Type I	Type I
0.5	Type I	Type I

both heterobilayers, which are compatible with the influence of the external electric field. Moreover, to observe the evolution of the band alignments of the heterobilayers, the layer-dependent projected electronic bands are considered, and these are exhibited in Fig. 9. As can be seen from Figs. 9 and 10, as the magnitude of the applied electric field is increased in the positive region, the VBM of the MoSSe moves toward the Fermi level, while the CBM shifts upward. However, the VBM and CBM of the MBP are scarcely changed by the positive electric field, which indicates that the MBP/MoSSe heterobilayer has

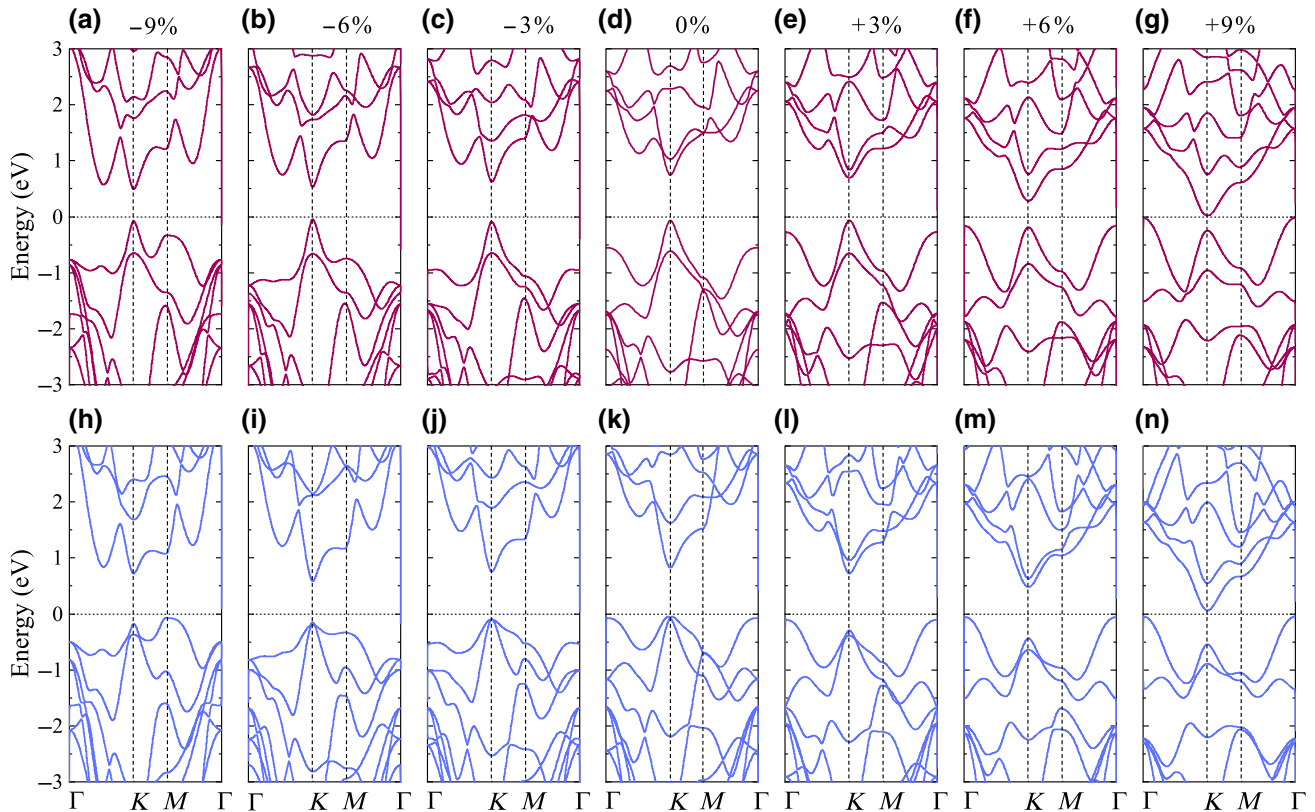


FIG. 11. Electronic band spectra of (a)–(g) MBP/MoSSe and (h)–(n) MoSSe/MBP under the influence of biaxial strain.

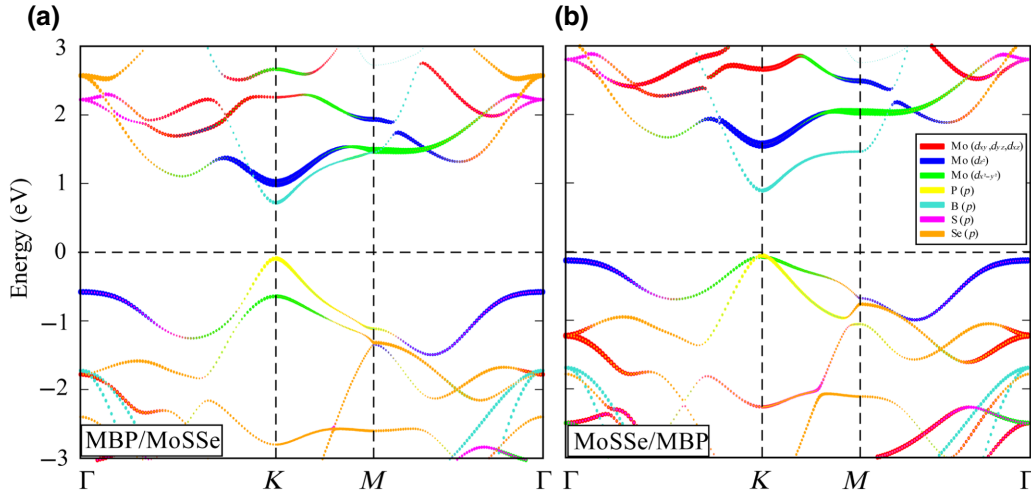


FIG. 12. Orbital-projected electronic band structures of pristine (a) MBP/MoSSe and (b) MoSSe/MBP heterobilayers.

not changed its band alignment and retains a type-I alignment in the positive-electric-field region. In the negative region of the electric field, the VBM of the MoSSe shifts below the Fermi level, while its CBM shifts toward the Fermi level, and the MBP behaves similarly to the way it behaves in the positive region. In addition, the MoSSe contributes significantly to the CBM at -0.4 and -0.5 V \AA^{-1} . The MBP/MoSSe heterobilayer transitions from a type-I to a type-II band alignment due to the MoSSe having a lower CBM and VBM than the MBP. On the other hand, in the MoSSe/MBP heterobilayer, the VBM and the CBM of the MBP shift upward between -0.5 and 0.5 V \AA^{-1} . At the same time, the VBM and CBM of the MoSSe slide downward indistinctly. Also, as exhibited in Fig. 10 and Table IV, the type-II alignment of the MoSSe/MBP heterobilayer is preserved between -0.5 and 0.1 V \AA^{-1} because the MoSSe and MBP contribute to the VBM and CBM, respectively. Since the MBP contributes to the VBM between 0.2 and 0.5 V \AA^{-1} , a transition of the band alignment from type II to type I occurs.

Furthermore, to demonstrate tunability of the electronic structures of both heterobilayers under compressive and tensile effects, an in-plane biaxial strain is considered. A biaxial strain from -9% to 9% with strain intervals of 3% is applied. A negative sign expresses a compressive strain, and a positive sign expresses a tensile strain. A

graph of the total energy versus the biaxial strain indicates that the pristine heterobilayers are energetically favorable, which is indicated in Fig. 7(d) [the inset of Fig. 7(d) represents the MoSSe/MBP heterobilayer]. The biaxial strain is defined as $(a - a_0)/a_0$, where a and a_0 are the lattice constants of the strained and the pristine heterobilayer, respectively. The variation of the band gap and the electronic band structure of both heterobilayers under biaxial strain is shown in Figs. 7(e) and 11, respectively. In the pristine condition, the CBM and VBM are located at the K point for the MBP (MoSSe)/MoSSe (MBP) heterobilayers. To describe precisely the electronic structures under a biaxial strain condition, we calculate the orbital-projected electronic band structures for both heterobilayers. As seen in Fig. 12, contributions to the CBM and VBM of the MBP/MoSSe heterobilayer are provided by the p orbitals of B and P atoms, respectively. The CBM of the MoSSe/MBP heterobilayer is contributed to by the p orbitals of the B atoms similarly to the MBP/MoSSe heterobilayer, while the $(d_{x^2-y^2})$ orbitals of Mo and the p orbitals of the P atoms contribute to the VBM. It is obvious from Fig. 7(e) that the band gap decreases for both heterobilayers with increasing tensile and compressive strain. In particular, as shown in Table V, with increasing tensile strain for the MBP (MoSSe)/MoSSe (MBP) heterobilayers, while the Se-Mo-S and B-P bond lengths increase, the

TABLE V. Change of bond lengths as a function of biaxial strain for MBP/MoSSe and MoSSe/MBP heterobilayers.

	MBP/MoSSe			MoSSe/MBP		
	$d_{\text{Mo-S}}$ (Å)	$d_{\text{Mo-Se}}$ (Å)	$d_{\text{B-P}}$ (Å)	$d_{\text{Mo-S}}$ (Å)	$d_{\text{Mo-Se}}$ (Å)	$d_{\text{B-P}}$ (Å)
-9%	2.361	2.496	1.725	2.361	2.496	1.732
-6%	2.375	2.503	1.751	2.377	2.505	1.758
-3%	2.393	2.513	1.807	2.393	2.514	1.808
0%	2.414	2.528	1.863	2.413	2.529	1.863
3%	2.438	2.548	1.919	2.438	2.549	1.920
6%	2.464	2.570	1.975	2.465	2.571	1.976
9%	2.490	2.597	2.031	2.492	2.597	2.032

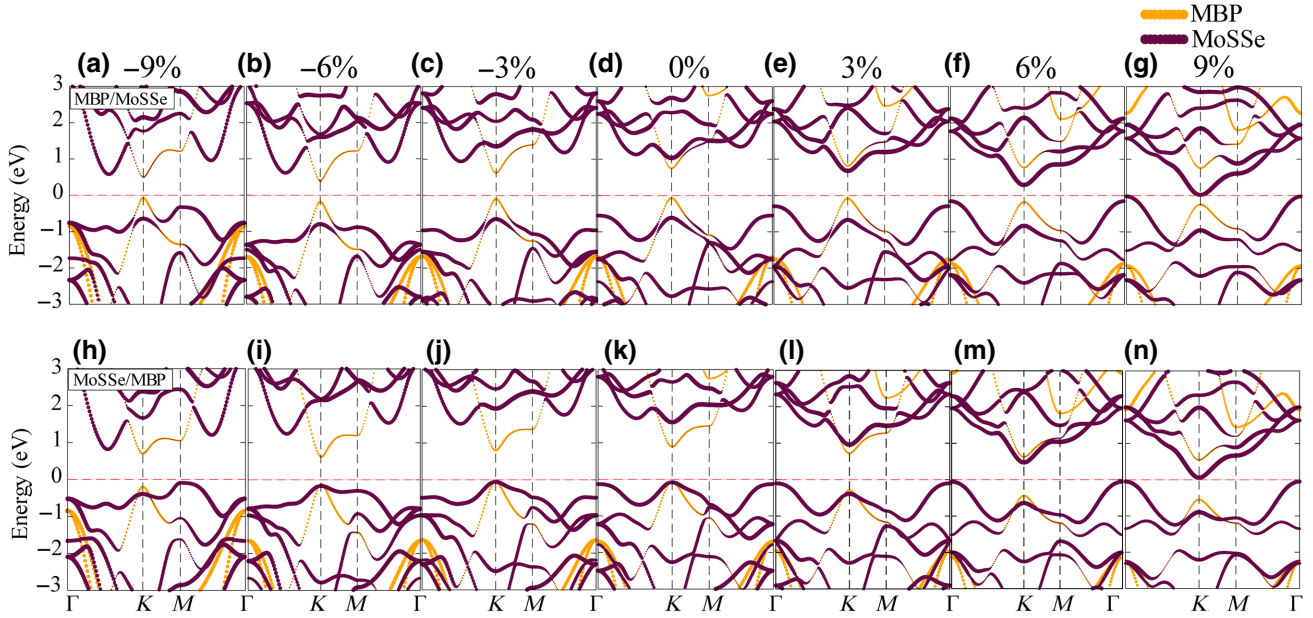


FIG. 13. Layer-dependent projected electronic band structures of MBP/MoSSe and MoSSe/MBP heterobilayers under the effect of biaxial strain.

bond angles reduce accordingly. With the reduction of the bond angles, while the coupling of the p and d_{z^2} orbitals weakens, the coupling between the p and $d_{x^2-y^2}$ orbitals strengthens. Because of the alterations in orbital coupling, the K point of the conduction band and the Γ point of the valence band shift toward the Fermi level. When the tensile strain reaches 6% (3%), the electronic bands become indirect, with a decreasing band gap for the MBP (MoSSe)/MoSSe (MBP) heterobilayers. In contrast to the case of tensile strain, with increasing compressive strain, the Se-Mo-S and B-P bond lengths decrease for both heterobilayers (see Table V), and the bond angles consequently increase. Because of the increased bond angles, while the coupling between the $d_{x^2-y^2}$ and p orbitals weakens, the coupling between the p and d_{z^2} orbitals strengthens. Therefore, the valence band at the M point and the conduction band between the Γ and K points are shifted toward the Fermi level. In addition, as also presented in Fig. 13, the CBM of the MoSSe is moved upward with increasing compressive strain due to the d_{z^2} orbitals. The direct-band-gap feature is preserved for all compressive-strain values for both heterobilayers except for the value of -9% for the MoSSe/MBP heterobilayer. Further, the evolution of the interlayer charge transfer as a function of biaxial strain is considered [Fig. 7(f)]. Predictably, the interlayer charge transfer varies insignificantly in the presence of biaxial strain due to the small changes in the interlayer distances of the heterobilayers. Furthermore, the evolution of the band alignments of the heterobilayers under biaxial strain is displayed in Fig. 14 and Table VI. As mentioned earlier, the biaxial strain induces weakening or strengthening of the coupling of the orbitals. Therefore, the

alterations of the orbitals are a reason for modifications of the electronic band structure that can directly change the band alignments of the heterobilayers. One can see in Fig. 14 that the band gap of the MoSSe in the presence of biaxial strain is higher than that of the MBP except for tensile strains of 6% and 9% for both heterobilayers. Hence, for a type-I band alignment, photogenerated electrons and holes migrate from MoSSe to MBP, leading to recombination. On the other hand, for a type-II band alignment, photogenerated electrons are transferred from the CBM of the MoSSe to the CBM of the MBP layer, while photogenerated holes are transferred from the VBM of the MBP layer to the VBM of the MoSSe layer.

Additionally, out-of-plane strain is considered for both heterobilayers. An out-of-plane strain from 0.2% to -0.2% is applied with strain intervals of 0.1%. The positive and negative signs denote tensile and compressive strains, respectively. From Figs. 7(g) and 3, a graph of the total energy versus the out-of-plane strain shows that the energetically favorable interlayer distance of MBP

TABLE VI. Variation of band alignments in the presence of biaxial strain.

Strain (%)	MBP/MoSSe	MoSSe/MBP
-9	Type I	Type II
-6	Type I	Type II
-3	Type I	Type II
0	Type I	Type II
3	Type II	Type II
6	Type I	Type I
9	Type I	Type I

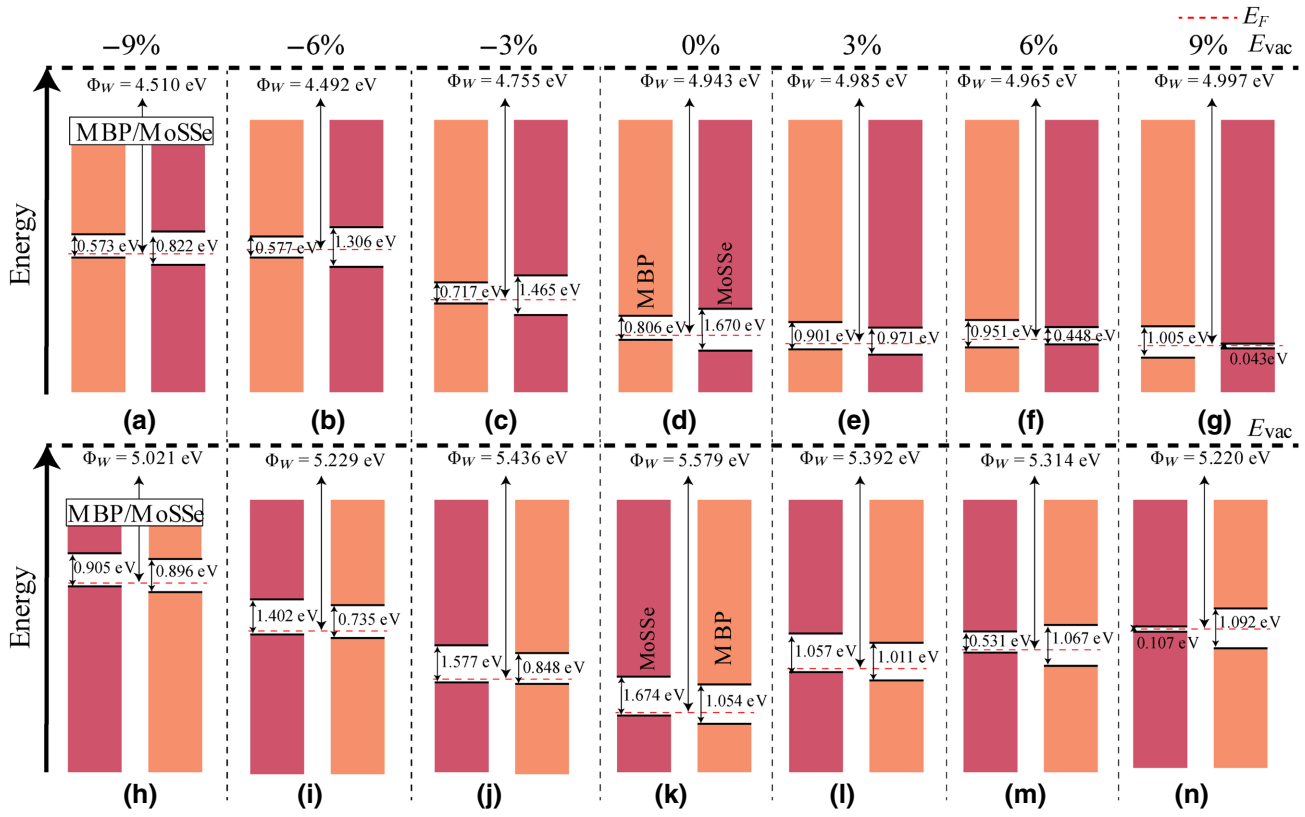


FIG. 14. Evolution of band alignments of MBP/MoSSe and MoSSe/MBP heterobilayers under the effect of biaxial strain.

(MoSSe)/MoSSe (MBP) is approximately 3.20 (3.43) Å. The evolution of the band gaps and electronic bands of both the MBP/MoSSe and the MoSSe/MBP heterobilayers

in the presence of out-of-plane strain is shown in Fig. 7(h) and Fig. 15. In circumstances in which out-of-plane strain is employed with vdW heterobilayers, there are two main

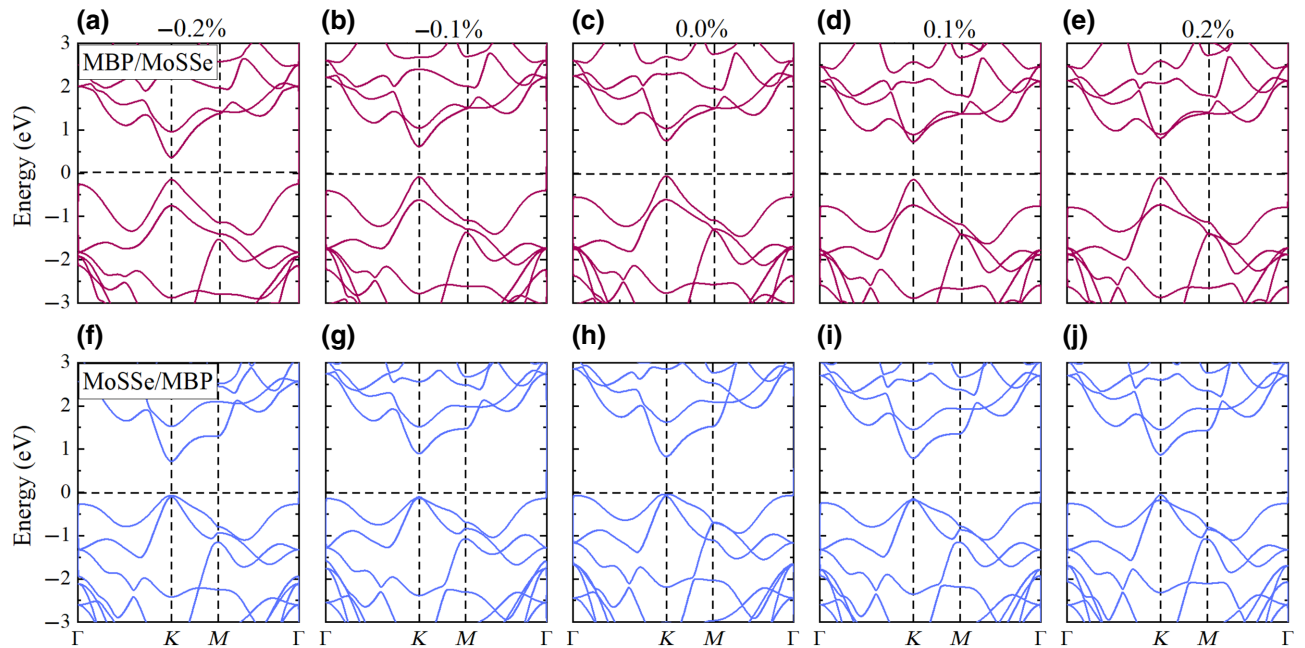


FIG. 15. Electronic band structure of (a)–(e) MBP/MoSSe and (f)–(j) MoSSe/MBP in the presence of out-of-plane strain.

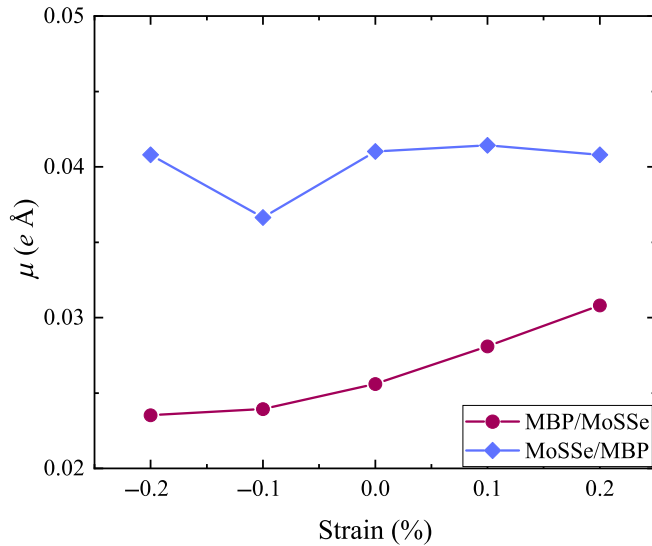


FIG. 16. Evolution of dipole moments of MBP/MoSSe and MoSSe/MBP heterobilayers in the presence of out-of-plane strain.

factors that can change the band gaps of heterobilayers: variation of the interlayer distances and of the dipole moments. The influence of the dipole moment on both heterobilayers is also studied, and is presented in Fig. 16. As shown in Figs. 7(h), 7(i), and 16, with increasing interlayer

distance and dipole moment, the charge transfer tends to diminish. Therefore, the electronic band gaps widen, and, meanwhile, the direct band gap is retained. In addition, it can be seen in Fig. 7(i) that the interlayer charge transfer between the MBP and MoSSe layers decreases when the tensile strain in the MoSSe/MBP heterobilayer reaches 0.2%. It can be said that this is a limit value at which the two monolayers begin to separate. Therefore, the contributions of both MBP and MoSSe to the electronic band are almost the same as in the case of the pristine form [see Fig. 17(j)]. It is also clearly seen that the interlayer distances in the MBP/MoSSe heterobilayer under an out-of-plane strain are narrower than those in the MoSSe/MBP heterobilayer. Therefore, the charge transfer is rather high in the MBP/MoSSe heterobilayer compared with the MoSSe/MBP heterobilayer. From Fig. 12, one can see that the CBM is contributed by the B atoms. As presented in Fig. 17, for the MBP/MoSSe heterobilayer, with increasing interlayer distance, the amount of charge transfer from the B atoms decreases, resulting in the CBM shifting upward from the Fermi level. On the other hand, in the MoSSe/MBP heterobilayer, the charge transfer from the B atoms increases with increasing compressive strain, and the CBM shifts to the Fermi level. As presented in Fig. 18 and Table VII, in the MBP/MoSSe heterobilayer, variation occurs in the electronic band structure in the presence of out-of-plane strain, yet the band alignment

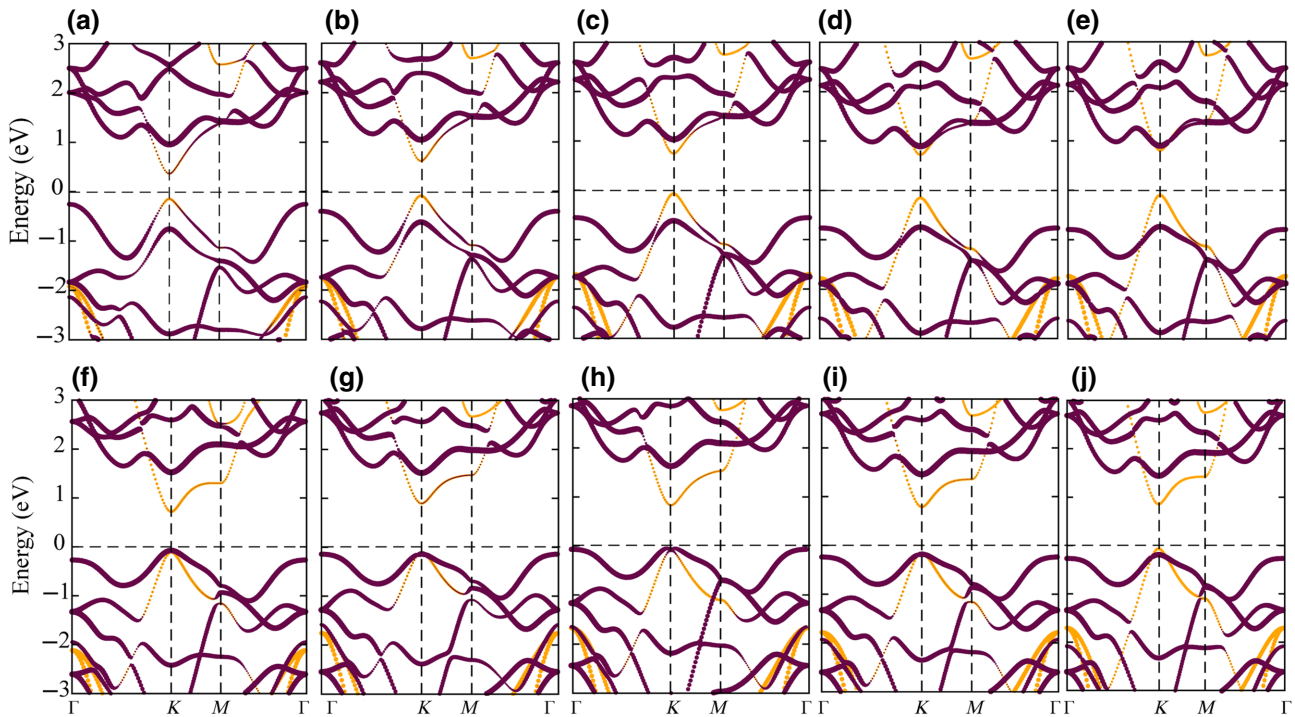


FIG. 17. Layer-dependent projected electronic band spectra under the effect of (a) -0.2% , (b) -0.1% , (c) 0.0% , (d) 0.1% , and (e) 0.2% out-of-plane strain for MBP/MoSSe heterobilayer and (f) -0.2% , (g) -0.1% , (h) 0.0% , (i) 0.1% , and (j) 0.2% out-of-plane strain for MoSSe/MBP heterobilayer.

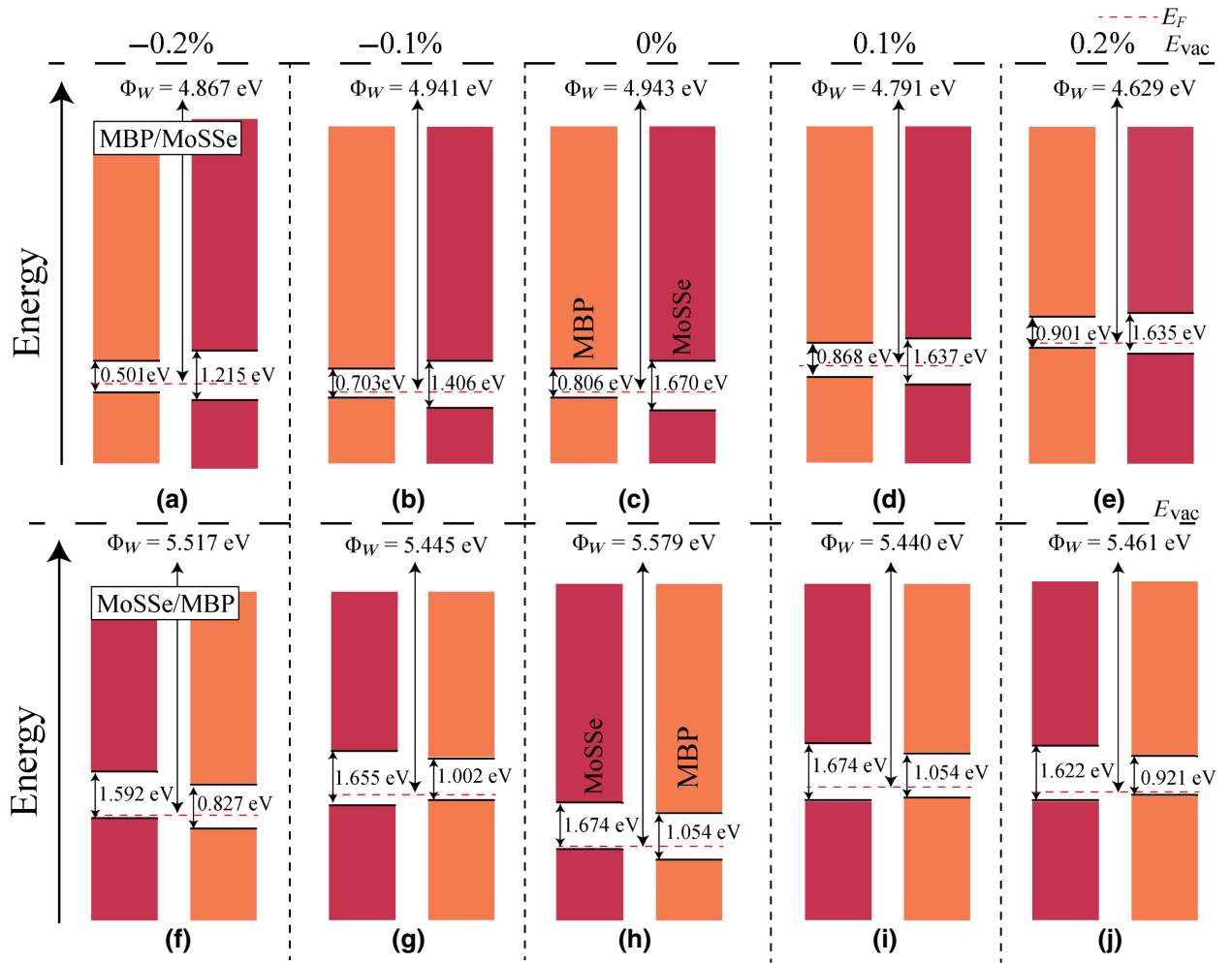


FIG. 18. Variation of band alignments of MBP/MoSSe and MoSSe/MBP heterobilayers under the effect of out-of-plane strain.

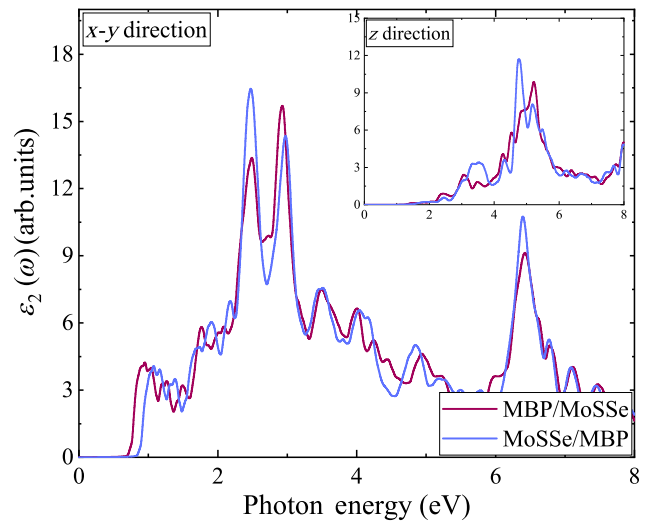
is not affected. For the MoSSe/MBP heterobilayer, both the electronic band structure and the band alignment are modified under the influence of out-of-plane strain.

B. Optical properties

In order to examine the effect of the layer order, external electric fields, and biaxial strain on the optical properties of MBP (MoSSe)/MoSSe (MBP) heterobilayers, the variation of the imaginary part of the dielectric function is calculated (Fig. 19). The imaginary part of the dielec-

TABLE VII. Variation of band alignments in the presence of out-of-plane strain.

Strain (%)	MBP/MoSSe	MoSSe/MBP
-0.2	Type I	Type II
-0.1	Type I	Type I
0	Type I	Type II
0.1	Type I	Type I
0.2	Type I	Type I


 FIG. 19. Frequency-dependent imaginary dielectric function $[\epsilon_2(\omega)]$ of MBP/MoSSe and MoSSe/MBP heterobilayers.

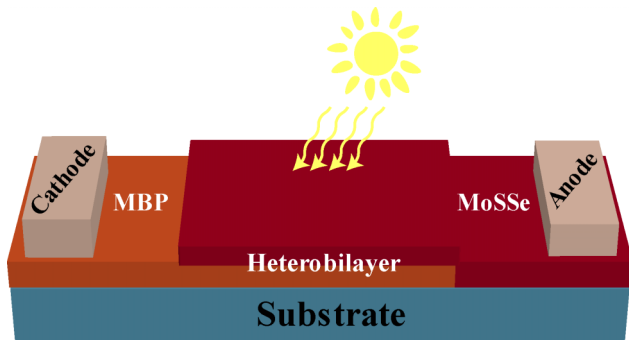


FIG. 20. Schematic representation of a MoSSe/MBP heterobilayer solar cell.

tric function is concerned with photon absorption, as mentioned in Sec. II. Since both heterobilayers have an anisotropy in the z direction, the imaginary part of the dielectric functions is considered in the in-plane (x - y) and out-of-plane (z) directions. The absorption onsets in the in-plane (out-of-plane) direction for pristine MBP/MoSSe and MoSSe/MBP are found to be 0.756 (1.096) and 0.877 eV (1.536 eV), respectively, which are compatible with the electronic band gaps. In the in-plane direction, there are three main absorption peaks situated in the visible and UV regions that are observed, at 2.51 (blue), 2.91

(violet), and 6.42 eV (UV) for the MBP/MoSSe heterobilayer, and at 2.48 (green), 2.94 (violet), and 6.43 eV (UV) for the MoSSe/MBP heterobilayer. The absorption in the visible light region observed along the in-plane direction implies high efficiency when the heterobilayers are utilized for solar energy conversion, which we illustrate in Fig. 20 for a MoSSe/MBP heterobilayer. Further, the imaginary part of the dielectric function of the MBP (MoSSe)/MoSSe (MBP) heterobilayers is investigated in the presence of an external electric field, as shown in Fig. 21. In the inset of Fig. 21, it can be observed that for both heterobilayers, while the intensity of the absorption peak at positive electric field values increases, it decreases at negative field values. Further, the imaginary parts of the dielectric function of the MBP (MoSSe)/MoSSe (MBP) heterobilayers versus the energy of the incident photons for compressive and tensile strains are presented in Fig. 22. The onset values for the MBP/MoSSe heterobilayer behave with respect to the values for MoSSe/MBP like those for the pristine states, and this result is also compatible with the strain-dependent band structures. When the tensile (compressive) strain is increased, a redshift (blueshift) occurs in the in-plane direction for both heterobilayers, with an increasing (decreasing) intensity of the main absorption peaks. Remarkably, the main out-of-plane absorption intensity for the imaginary part of the dielectric function decreases as the tensile strain

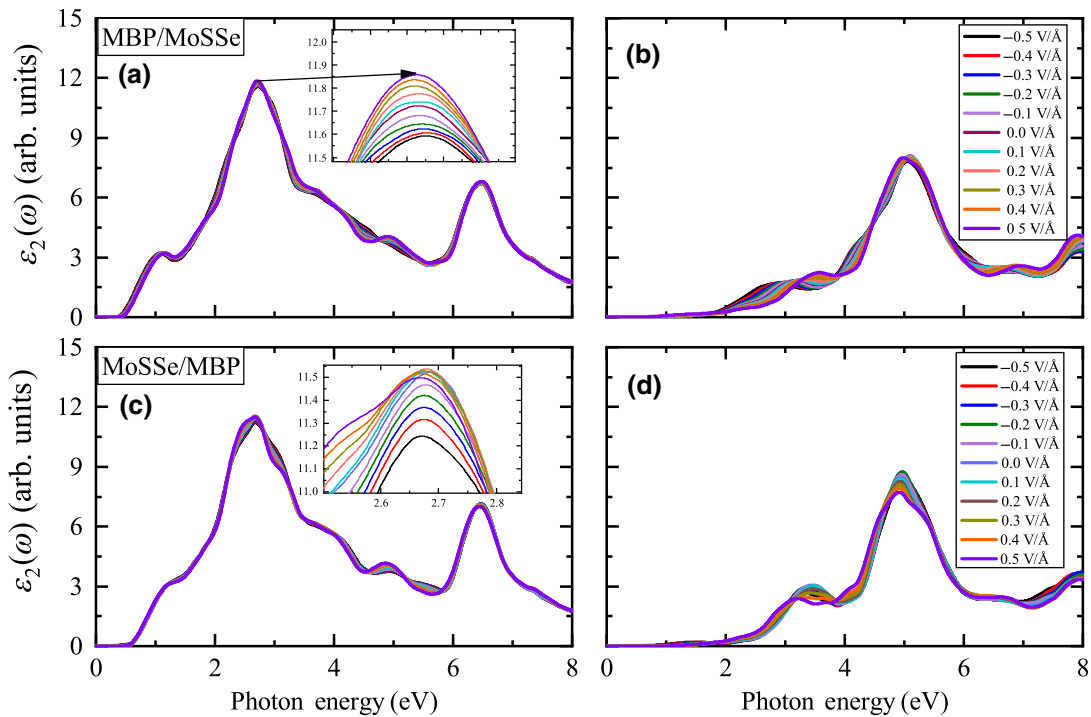


FIG. 21. Frequency-dependent imaginary dielectric functions of MBP/MoSSe for (a) x - y , (b) z directions, and MoSSe/MBP (c) x - y , (d) z directions under an external perpendicular electric field.

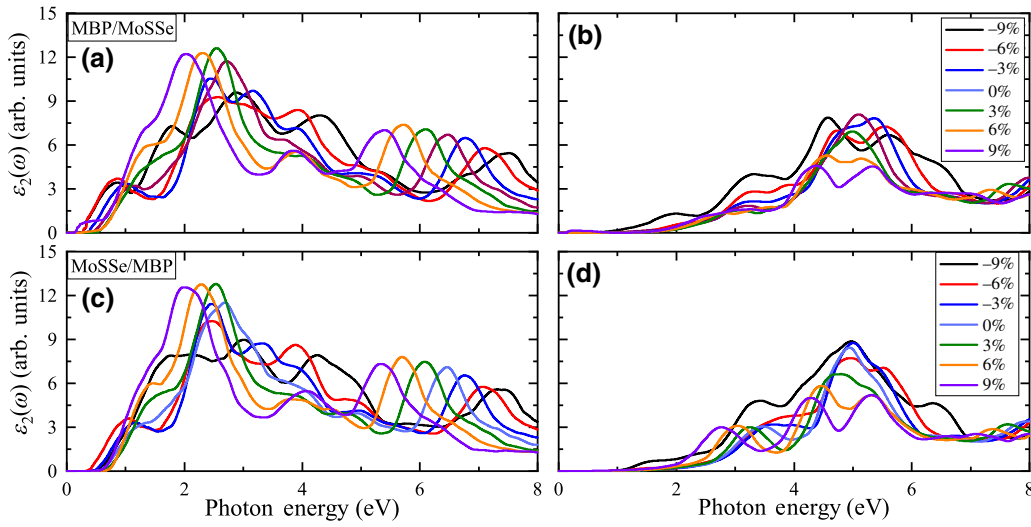


FIG. 22. Frequency-dependent imaginary dielectric functions of MBP/MoSSe for (a) x - y , (b) z directions, and MoSSe/MBP (c) x - y , (d) z directions under the effect of biaxial strain.

increases, while it increases when the compressive strain increases.

Furthermore, the evolution of the imaginary part of the dielectric function under the influence of an out-of-plane strain is investigated and is displayed in Fig. 23. In the presence of an out-of-plane strain, it is observed that the imaginary part of the dielectric function in the in-plane direction for both the MBP/MoSSe and the MoSSe/MBP heterobilayers is altered only slightly compared with the results for an in-plane biaxial strain.

IV. CONCLUSION

In summary, we study heterobilayers made from MBP and Janus MoSSe under the effects of strain and electric fields. Six possible stackings of the heterobilayers are considered for each heterobilayer. Two stable MBP (MoSSe)/MoSSe (MBP) heterobilayers with minimum

energy also have a direct band gap. To describe the intrinsic electric field created in the interlayer of the heterobilayer, the dipole moments and electrostatic potentials are considered. Moreover, considering the results of Bader analysis for both heterobilayers, it is seen that charge is transferred from the single-layer boron phosphide to the Janus MoSSe. Thus, it is indicated that the intrinsic electric field is directed from the MoSSe layer to the MBP layer for both heterobilayers. While the MBP/MoSSe bilayer is type I without the application of an electric field or strain, it is type II when these are applied. It is observed that the band alignments of the MBP/MoSSe and MoSSe/MBP heterobilayers in the presence of an external perpendicular electric field are changed between -0.4 and -0.5 V \AA^{-1} and between 0.1 and 0.5 V \AA^{-1} , respectively. Under in-plane and out-of-plane strains, the band alignment of the MBP/MoSSe heterobilayer is preserved. On the other hand, the band alignment of the MoSSe/MBP heterobilayer is preserved except for values of 6% and 9% of

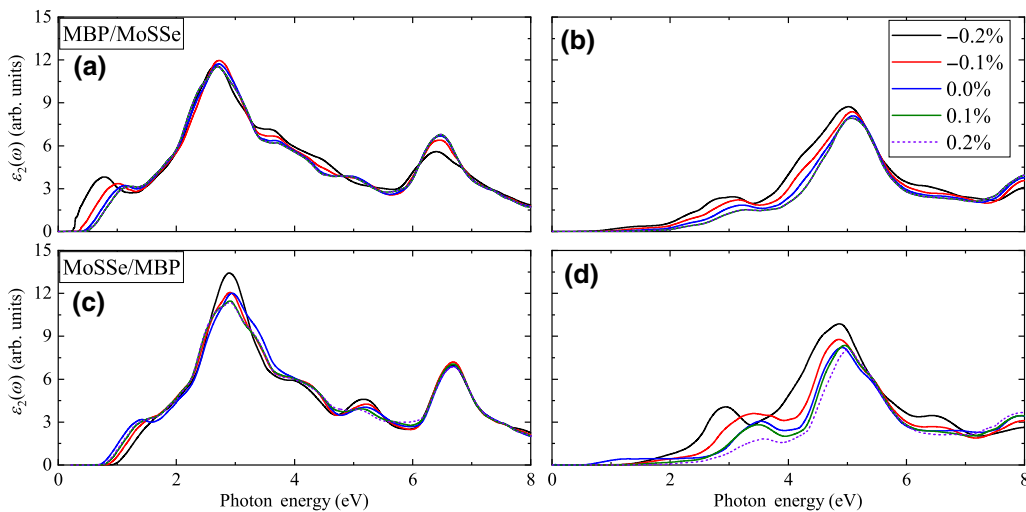


FIG. 23. Frequency-dependent imaginary dielectric functions of MBP/MoSSe for (a) x - y and (b) z directions, and of MoSSe/MBP for (c) x - y and (d) z directions under the effect of out-of-plane strain.

the in-plane strain. Moreover, the band alignment of the MoSSe/MBP heterobilayer is altered under out-of-plane strain. Preserving band alignments under the influence of external electric fields and strain provides freedom in the design of optoelectronic devices.

ACKNOWLEDGMENTS

Y.M. and R.C. acknowledge Ankara University for use of the high-performance computing facility through the AYP (Grant No. 17A0443001) and also acknowledge the TUBITAK ULAKBIM High Performance and Grid Computing Center (TR-Grid e-Infrastructure).

APPENDIX

APPENDIX: PROPOSED EXPERIMENTAL PROCEDURE FOR MBP/MoSSe HETEROBILAYERS

Similarly to the process for MoS₂/WS₂ [96] heterobilayers proposed by Yuan and coworkers, the liquid-transfer technique can be used to synthesize MBP (MoSSe)/MoSSe (MBP) heterobilayers. The procedure for synthesis of the proposed heterobilayers is illustrated step by step in Fig. 24. To synthesize a MBP (MoSSe)/MoSSe (MBP) heterobilayer, firstly, MBP is grown on a SiC substrate and MoSSe on a sapphire substrate by the CVD method. A spin-coating process is applied to the surfaces of

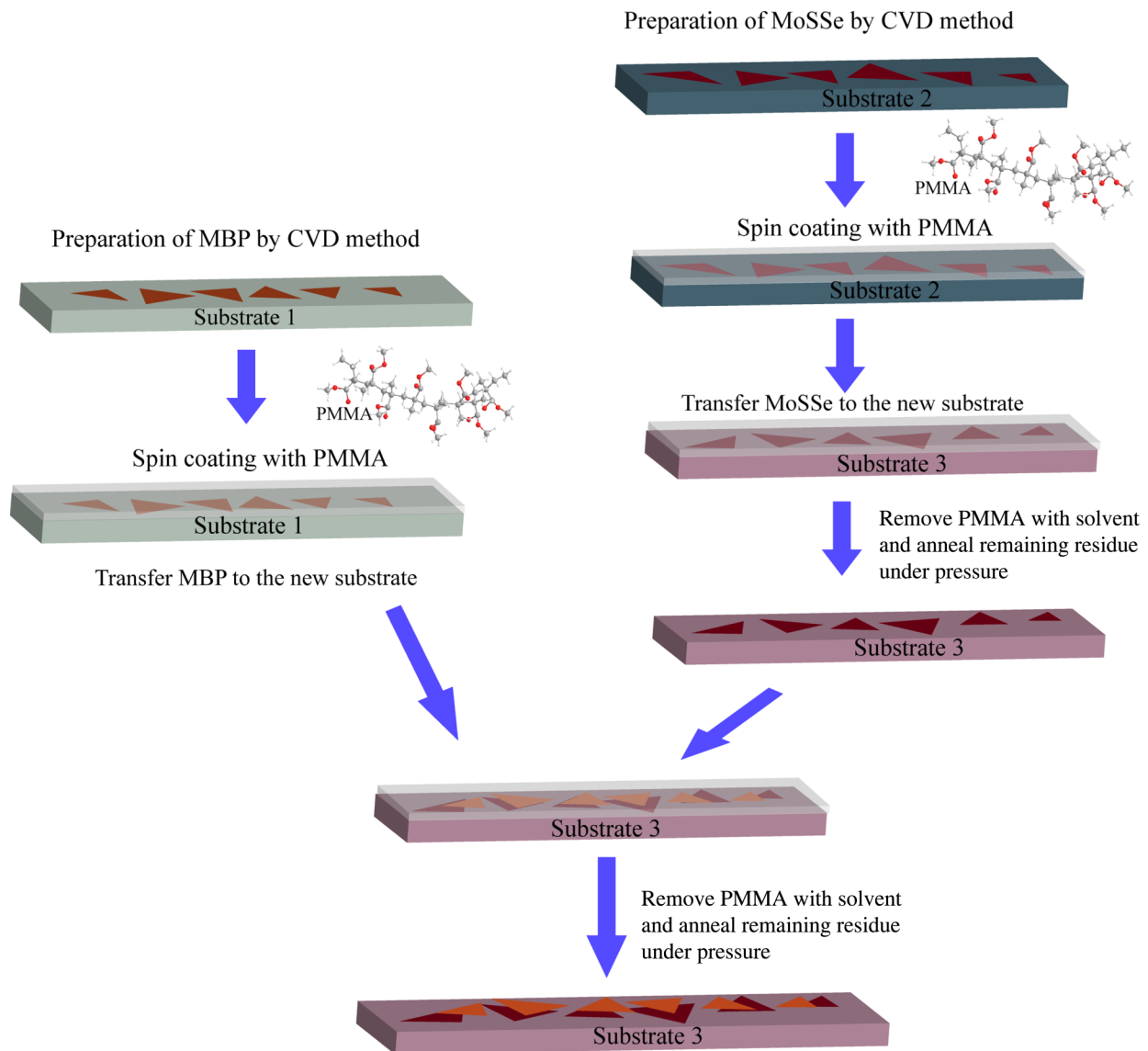


FIG. 24. Schematic representation of the synthesis of MBP (MoSSe)/MoSSe (MBP) heterobilayers using the proposed liquid-transfer technique.

the materials to stack the MBP and MoSSe monolayers produced by the CVD method. To coat the two monolayers, poly(methyl methacrylate) (PMMA) is used. Then, NaOH solution is used as an etchant to remove the MoSSe monolayer from substrate 2. The removed sample is transferred to substrate 3. After transportation of the MoSSe monolayer to substrate 3, the PMMA coating is removed with a solvent such as dimethylformamide (DMF). The remaining residues are annealed under pressure. In addition, similarly to the MoSSe monolayer, the MBP is coated with PMMA and etched with NaOH solution from substrate 1. Then the MBP is stacked on monolayer MoSSe on substrate 3. After removing the PMMA with DMF, the remaining residues are completely removed from the heterobilayer by a second annealing process.

-
- [1] D. Tománek, Collection on two-dimensional materials and devices, *Phys. Rev. Mater.* **4**, 030001 (2020).
- [2] G. Xie, Z. Ju, K. Zhou, X. Wei, Z. Guo, Y. Cai, and G. Zhang, Ultra-low thermal conductivity of two-dimensional phononic crystals in the incoherent regime, *Npj Comput. Mater.* **4**, 1 (2018).
- [3] W. Yin, B. Wen, Q. Ge, D. Zou, Y. Xu, M. Liu, X. Wei, M. Chen, and X. Fan, Role of intrinsic dipole on photocatalytic water splitting for janus mosse/nitrides heterostructure: A first-principles study, *Prog. Nat. Sci.: Mater. Int.* **29**, 335 (2019).
- [4] B. Radisavljevic, A. Radenovic, J. Brivio, V. Giacometti, and A. Kis, Single-layer mos 2 transistors, *Nat. Nanotechnol.* **6**, 147 (2011).
- [5] K. F. Mak, C. Lee, J. Hone, J. Shan, and T. F. Heinz, Atomically Thin mos 2: A new Direct-Gap Semiconductor, *Phys. Rev. Lett.* **105**, 136805 (2010).
- [6] A. Splendiani, L. Sun, Y. Zhang, T. Li, J. Kim, C.-Y. Chim, G. Galli, and F. Wang, Emerging photoluminescence in monolayer mos2, *Nano Lett.* **10**, 1271 (2010).
- [7] H. Zeng, J. Dai, W. Yao, D. Xiao, and X. Cui, Valley polarization in mos 2 monolayers by optical pumping, *Nat. Nanotechnol.* **7**, 490 (2012).
- [8] Q. H. Wang, K. Kalantar-Zadeh, A. Kis, J. N. Coleman, and M. S. Strano, Electronics and optoelectronics of two-dimensional transition metal dichalcogenides, *Nat. Nanotechnol.* **7**, 699 (2012).
- [9] K. S. Novoselov, A. K. Geim, S. V. Morozov, D. Jiang, Y. Zhang, S. V. Dubonos, I. V. Grigorieva, and A. A. Firsov, Electric field effect in atomically thin carbon films, *Science* **306**, 666 (2004).
- [10] A. Kormányos, G. Burkard, M. Gmitra, J. Fabian, V. Zólyomi, N. D. Drummond, and V. Fal'ko, $k \cdot p$ theory for two-dimensional transition metal dichalcogenide semiconductors, *2D Materials* **2**, 022001 (2015).
- [11] K. F. Mak and J. Shan, Photonics and optoelectronics of 2d semiconductor transition metal dichalcogenides, *Nat. Photonics* **10**, 216 (2016).
- [12] H. M. Hill, A. F. Rigosi, K. T. Rim, G. W. Flynn, and T. F. Heinz, Band alignment in mos2/ws2 transition metal dichalcogenide heterostructures probed by scanning tunneling microscopy and spectroscopy, *Nano Lett.* **16**, 4831 (2016).
- [13] H. Liu, A. T. Neal, Z. Zhu, Z. Luo, X. Xu, D. Tománek, and P. D. Ye, Phosphorene: An unexplored 2d semiconductor with a high hole mobility, *ACS Nano* **8**, 4033 (2014).
- [14] L. Li, Y. Yu, G. J. Ye, Q. Ge, X. Ou, H. Wu, D. Feng, X. H. Chen, and Y. Zhang, Black phosphorus field-effect transistors, *Nat. Nanotechnol.* **9**, 372 (2014).
- [15] A. Mogulkoc, Y. Mogulkoc, A. N. Rudenko, and M. I. Katsnelson, Polaronic effects in monolayer black phosphorus on polar substrates, *Phys. Rev. B* **93**, 085417 (2016).
- [16] M. Buscema, D. J. Groenendijk, S. I. Blanter, G. A. Steele, H. S. Van Der Zant, and A. Castellanos-Gomez, Fast and broadband photoresponse of few-layer black phosphorus field-effect transistors, *Nano Lett.* **14**, 3347 (2014).
- [17] R. Fei and L. Yang, Strain-engineering the anisotropic electrical conductance of few-layer black phosphorus, *Nano Lett.* **14**, 2884 (2014).
- [18] C. R. Espinoza, D. Ryndyk, A. Dianat, R. Gutierrez, and G. Cuniberti, First principles study of field effect device through van der waals and lateral heterostructures of graphene, phosphorene and graphane, *Nano Materials Science* (2021).
- [19] A. K. Geim and I. V. Grigorieva, Van der waals heterostructures, *Nature* **499**, 419 (2013).
- [20] C. Xia, J. Du, M. Li, X. Li, X. Zhao, T. Wang, and J. Li, Effects of Electric Field on the Electronic Structures of Broken-Gap phosphorene/sn x 2 ($x = s, se$) van der Waals Heterojunctions, *Phys. Rev. Appl.* **10**, 054064 (2018).
- [21] C. Zhi, Y. Bando, C. Tang, H. Kuwahara, and D. Golberg, Large-scale fabrication of boron nitride nanosheets and their utilization in polymeric composites with improved thermal and mechanical properties, *Adv. Mater.* **21**, 2889 (2009).
- [22] A. Nag, K. Raidongia, K. P. Hembam, R. Datta, U. V. Waghmare, and C. Rao, Graphene analogues of bn: Novel synthesis and properties, *ACS Nano* **4**, 1539 (2010).
- [23] E. Hernandez, C. Goze, P. Bernier, and A. Rubio, Elastic Properties of c and b x c y n z Composite Nanotubes, *Phys. Rev. Lett.* **80**, 4502 (1998).
- [24] A. P. Suryavanshi, M.-F. Yu, J. Wen, C. Tang, and Y. Bando, Elastic modulus and resonance behavior of boron nitride nanotubes, *Appl. Phys. Lett.* **84**, 2527 (2004).
- [25] H. Şahin, S. Cahangirov, M. Topsakal, E. Bekaroglu, E. Akturk, R. T. Senger, and S. Ciraci, Monolayer honeycomb structures of group-iv elements and iii-v binary compounds: First-principles calculations, *Phys. Rev. B* **80**, 155453 (2009).
- [26] K. Watanabe, T. Taniguchi, and H. Kanda, Direct-bandgap properties and evidence for ultraviolet lasing of hexagonal boron nitride single crystal, *Nat. Mater.* **3**, 404 (2004).
- [27] Y. Shi, C. Hamsen, X. Jia, K. K. Kim, A. Reina, M. Hofmann, A. L. Hsu, K. Zhang, H. Li, and Z.-Y. Juang *et al.*, Synthesis of few-layer hexagonal boron nitride thin film by chemical vapor deposition, *Nano Lett.* **10**, 4134 (2010).

- [28] A. Mogulkoc, Y. Mogulkoc, M. Modarresi, and B. Alkan, Electronic structure and optical properties of novel monolayer gallium nitride and boron phosphide heterobilayers, *Phys. Chem. Chem. Phys.* **20**, 28124 (2018).
- [29] D. Çakır, D. Kecik, H. Sahin, E. Durgun, and F. M. Peeters, Realization of ap-n junction in a single layer boron-phosphide, *Phys. Chem. Chem. Phys.* **17**, 13013 (2015).
- [30] B. Onat, L. Hallioglu, S. İpek, and E. Durgun, Tuning electronic properties of monolayer hexagonal boron phosphide with group iii-iv-v dopants, *J. Phys. Chem. C* **121**, 4583 (2017).
- [31] A. S. Rodin, A. Carvalho, and A. H. Castro Neto, Strain-Induced gap Modification in Black Phosphorus, *Phys. Rev. Lett.* **112**, 176801 (2014).
- [32] A. López-Castillo, Prediction of boron-phosphorous nanographene-like material, *Int. J. Quantum Chem.* **112**, 3152 (2012).
- [33] Y. Wang and S. Shi, Structural and electronic properties of monolayer hydrogenated honeycomb iii-v sheets from first-principles, *Solid State Commun.* **150**, 1473 (2010).
- [34] M. Wu, X. Wu, Y. Pei, and X. C. Zeng, Inorganic nanoribbons with unpassivated zigzag edges: Half metallicity and edge reconstruction, *Nano Res.* **4**, 233 (2011).
- [35] Z. Sohbatzadeh, M. Roknabadi, N. Shahtahmasebi, and M. Behdani, Spin-dependent transport properties of an arm-chair boron-phosphide nanoribbon embedded between two graphene nanoribbon electrodes, *Phys. E: Low-Dimens. Syst. Nanostruct.* **65**, 61 (2015).
- [36] J. Dong, H. Li, and L. Li, Multi-functional nano-electronics constructed using boron phosphide and silicon carbide nanoribbons, *NPG Asia Mater.* **5**, e56 (2013).
- [37] H. Shi, H. Pan, Y.-W. Zhang, and B. I. Yakobson, Quasiparticle band structures and optical properties of strained monolayer mos 2 and ws 2, *Phys. Rev. B* **87**, 155304 (2013).
- [38] Q. Yue, J. Kang, Z. Shao, X. Zhang, S. Chang, G. Wang, S. Qin, and J. Li, Mechanical and electronic properties of monolayer mos2 under elastic strain, *Phys. Lett. A* **376**, 1166 (2012).
- [39] R. Fivaz and E. Mooser, Mobility of charge carriers in semiconducting layer structures, *Phys. Rev.* **163**, 743 (1967).
- [40] M. Idrees, H. Din, R. Ali, G. Rehman, T. Hussain, C. Nguyen, I. Ahmad, and B. Amin, Optoelectronic and solar cell applications of janus monolayers and their van der waals heterostructures, *Phys. Chem. Chem. Phys.* **21**, 18612 (2019).
- [41] A. Mogulkoc, Y. Mogulkoc, S. Jahangirov, and E. Durgun, Characterization and stability of janus tixy (x/y= s, se, and te) monolayers, *J. Phys. Chem. C* **123**, 29922 (2019).
- [42] A.-Y. Lu, H. Zhu, J. Xiao, C.-P. Chuu, Y. Han, M.-H. Chiu, C.-C. Cheng, C.-W. Yang, K.-H. Wei, and Y. Yang *et al.*, Janus monolayers of transition metal dichalcogenides, *Nat. Nanotechnol.* **12**, 744 (2017).
- [43] X. Ma, X. Wu, H. Wang, and Y. Wang, A janus mosse monolayer: A potential wide solar-spectrum water-splitting photocatalyst with a low carrier recombination rate, *J. Mater. Chem. A* **6**, 2295 (2018).
- [44] Z. Guan, S. Ni, and S. Hu, Tunable electronic and optical properties of monolayer and multilayer janus mosse as a photocatalyst for solar water splitting: A first-principles study, *J. Phys. Chem. C* **122**, 6209 (2018).
- [45] C. Xia, W. Xiong, J. Du, T. Wang, Y. Peng, and J. Li, Universality of electronic characteristics and photocatalyst applications in the two-dimensional janus transition metal dichalcogenides, *Phys. Rev. B* **98**, 165424 (2018).
- [46] Y. Luo, S. Wang, H. Shu, J.-P. Chou, K. Ren, J. Yu, and M. Sun, A mosse/blue phosphorene vdw heterostructure with energy conversion efficiency of 19.9% for photocatalytic water splitting, *Semicond. Sci. Technol.* **35**, 125008 (2020).
- [47] R. Peng, Y. Ma, S. Zhang, B. Huang, and Y. Dai, Valley polarization in janus single-layer mosse via magnetic doping, *J. Phys. Chem. Lett.* **9**, 3612 (2018).
- [48] C. Zhang, Y. Nie, S. Sanvito, and A. Du, First-principles prediction of a room-temperature ferromagnetic janus vsse monolayer with piezoelectricity, ferroelasticity, and large valley polarization, *Nano Lett.* **19**, 1366 (2019).
- [49] D. Chen, X. Lei, Y. Wang, S. Zhong, G. Liu, B. Xu, and C. Ouyang, Tunable electronic structures in bp/mosse van der waals heterostructures by external electric field and strain, *Appl. Surf. Sci.* **497**, 143809 (2019).
- [50] Z. Cui, K. Bai, Y. Ding, X. Wang, E. Li, J. Zheng, and S. Wang, Electronic and optical properties of janus mosse and zno vdws heterostructures, Superlattices and Microstructures, 106445 (2020).
- [51] D. Xu, B. Zhai, Q. Gao, T. Wang, J. Li, and C. Xia, Interface-controlled band alignment transition and optical properties of janus mosse/gan vdw heterobilayers, *J. Phys. D: Appl. Phys.* **53**, 055104 (2019).
- [52] F. Li, W. Wei, P. Zhao, B. Huang, and Y. Dai, Electronic and optical properties of pristine and vertical and lateral heterostructures of janus mosse and wsse, *J. Phys. Chem. Lett.* **8**, 5959 (2017).
- [53] Y. Li, J. Wang, B. Zhou, F. Wang, Y. Miao, J. Wei, B. Zhang, and K. Zhang, Tunable interlayer coupling and schottky barrier in graphene and janus mosse heterostructures by applying an external field, *Phys. Chem. Chem. Phys.* **20**, 24109 (2018).
- [54] T. Jing, D. Liang, J. Hao, M. Deng, and S. Cai, Interface schottky barrier in hf 2 nt 2/msse (t= f, o, oh; m= mo, w) heterostructures, *Phys. Chem. Chem. Phys.* **21**, 5394 (2019).
- [55] H. U. Din, M. Idrees, A. Albar, M. Shafiq, I. Ahmad, C. V. Nguyen, and B. Amin, Rashba spin splitting and photocatalytic properties of gec- m sse (m= mo, w) van der waals heterostructures, *Phys. Rev. B* **100**, 165425 (2019).
- [56] V. O. Özcelik, J. G. Azadani, C. Yang, S. J. Koester, and T. Low, Band alignment of two-dimensional semiconductors for designing heterostructures with momentum space matching, *Phys. Rev. B* **94**, 035125 (2016).
- [57] T. Yamaha, S. Shibayama, T. Asano, K. Kato, M. Sakashita, W. Takeuchi, O. Nakatsuka, and S. Zaima, Experimental observation of type-i energy band alignment in lattice-matched ge1-x-y si x sn y/ge heterostructures, *Appl. Phys. Lett.* **108**, 061909 (2016).
- [58] S. Nakamura, M. Senoh, N. Iwasa, and S.-i. Nagahama, High-brightness ingan blue, green and yellow light-emitting diodes with quantum well structures, *Jpn. J. Appl. Phys.* **34**, L797 (1995).

- [59] Y. Shirasaki, G. J. Supran, M. G. Bawendi, and V. Bulović, Emergence of colloidal quantum-dot light-emitting technologies, *Nat. Photonics* **7**, 13 (2013).
- [60] C. Palacios-Berraquero, in *Quantum Confined Excitons in 2-Dimensional Materials* (Springer, Cambridge, UK, 2018), p. 71.
- [61] F. Withers, O. Del Pozo-Zamudio, A. Mishchenko, A. Rooney, A. Gholinia, K. Watanabe, T. Taniguchi, S. Haigh, A. Geim, and A. Tartakovskii *et al.*, Light-emitting diodes by band-structure engineering in van der waals heterostructures, *Nat. Mater.* **14**, 301 (2015).
- [62] V. Klimov, A. Mikhailovsky, S. Xu, A. Malko, J. Hollingsworth, a. C. Leatherdale, H.-J. Eisler, and M. Bawendi, Optical gain and stimulated emission in nanocrystal quantum dots, *Science* **290**, 314 (2000).
- [63] M. Grau, C. Lin, O. Dier, C. Lauer, and M.-C. Amann, Room-temperature operation of $3.26 \mu\text{m}$ gasb-based type-i lasers with quinary algaingssb barriers, *Appl. Phys. Lett.* **87**, 241104 (2005).
- [64] M. Idrees, C. V. Nguyen, H. Bui, and B. Amin, Electronic and optoelectronic properties of van der waals heterostructure based on graphene-like gan, blue phosphorene, sic, and zno: A first principles study, *J. Appl. Phys.* **127**, 245302 (2020).
- [65] O. E. Semonin, J. M. Luther, S. Choi, H.-Y. Chen, J. Gao, A. J. Nozik, and M. C. Beard, Peak external photocurrent quantum efficiency exceeding 100% via meg in a quantum dot solar cell, *Science* **334**, 1530 (2011).
- [66] E. M. Sanehira, A. R. Marshall, J. A. Christians, S. P. Harvey, P. N. Ciesielski, L. M. Wheeler, P. Schulz, L. Y. Lin, M. C. Beard, and J. M. Luther, Enhanced mobility csbpi3 quantum dot arrays for record-efficiency, high-voltage photovoltaic cells, *Sci. Adv.* **3**, eaao4204 (2017).
- [67] M. M. Furchi, F. Höller, L. Dobusch, D. K. Polyushkin, S. Schuler, and T. Mueller, Device physics of van der waals heterojunction solar cells, *Npj 2D Mater. Appl.* **2**, 1 (2018).
- [68] T. Xu, Y. Wang, X. Zhou, X. Zheng, Q. Xu, Z. Chen, Y. Ren, and B. Yan, Fabrication and assembly of two-dimensional tio₂/wo₃·h₂o heterostructures with type ii band alignment for enhanced photocatalytic performance, *Appl. Surf. Sci.* **403**, 564 (2017).
- [69] S. A. Rawool, M. R. Pai, A. M. Banerjee, A. Arya, R. Ningthoujam, R. Tewari, R. Rao, B. Chalke, P. Ayyub, and A. Tripathi *et al.*, pn heterojunctions in nio: Tio₂ composites with type-ii band alignment assisting sunlight driven photocatalytic h₂ generation, *Appl. Catal. B: Environ.* **221**, 443 (2018).
- [70] B.-X. Zhou, S.-S. Ding, Y. Wang, X.-R. Wang, W.-Q. Huang, K. Li, and G.-F. Huang, Type-ii/type-ii band alignment to boost spatial charge separation: A case study of gc 3 n 4 quantum dots/a-tio 2/r-tio 2 for highly efficient photocatalytic hydrogen and oxygen evolution, *Nanoscale* **12**, 6037 (2020).
- [71] R. Yan, S. Fathipour, Y. Han, B. Song, S. Xiao, M. Li, N. Ma, V. Protasenko, D. A. Muller, and D. Jena *et al.*, Esaki diodes in van der waals heterojunctions with broken-gap energy band alignment, *Nano Lett.* **15**, 5791 (2015).
- [72] J. Shim, S. Oh, D.-H. Kang, S.-H. Jo, M. H. Ali, W.-Y. Choi, K. Heo, J. Jeon, S. Lee, and M. Kim *et al.*, Phosphorene/rhenium disulfide heterojunction-based negative differential resistance device for multi-valued logic, *Nat. Commun.* **7**, 1 (2016).
- [73] Q. Li, K.-Q. Chen, and L.-M. Tang, Large Valley Splitting in van der Waals Heterostructures with Type-iii Band Alignment, *Phys. Rev. Appl.* **13**, 014064 (2020).
- [74] C. Shang, B. Xu, X. Lei, S. Yu, D. Chen, M. Wu, B. Sun, G. Liu, and C. Ouyang, Bandgap tuning in mosse bilayers: Synergistic effects of dipole moment and interlayer distance, *Phys. Chem. Chem. Phys.* **20**, 20919 (2018).
- [75] H. R. Jappor, M. M. Obeid, T. V. Vu, D. Hoat, H. D. Bui, N. N. Hieu, S. J. Edrees, Y. Mogulkoc, and R. Khenata, Engineering the optical and electronic properties of janus monolayer ga₂ss_e by biaxial strain, *Superlattices Microstruct.* **130**, 545 (2019).
- [76] R. Caglayan, Y. Mogulkoc, A. Mogulkoc, and B. Alkan, First principles study on optoelectronic properties of energetically stable si/ins van der waals heterobilayers, *J. Mater. Sci.* **55**, 15199 (2020).
- [77] P. E. Blöchl, Projector augmented-wave method, *Phys. Rev. B* **50**, 17953 (1994).
- [78] G. Kresse and J. Hafner, Ab initio molecular dynamics for liquid metals, *Phys. Rev. B* **47**, 558 (1993).
- [79] G. Kresse and J. Hafner, Ab initio molecular-dynamics simulation of the liquid-metal–amorphous-semiconductor transition in germanium, *Phys. Rev. B* **49**, 14251 (1994).
- [80] G. Kresse and J. Furthmüller, Efficiency of ab-initio total energy calculations for metals and semiconductors using a plane-wave basis set, *Comput. Mater. Sci.* **6**, 15 (1996).
- [81] G. Kresse and J. Furthmüller, Efficient iterative schemes for ab initio total-energy calculations using a plane-wave basis set, *Phys. Rev. B* **54**, 11169 (1996).
- [82] J. P. Perdew, K. Burke, and M. Ernzerhof, Generalized Gradient Approximation Made Simple, *Phys. Rev. Lett.* **77**, 3865 (1996).
- [83] H. J. Monkhorst and J. D. Pack, Special points for brillouin-zone integrations, *Phys. Rev. B* **13**, 5188 (1976).
- [84] S. Grimme, Semiempirical gga-type density functional constructed with a long-range dispersion correction, *J. Comput. Chem.* **27**, 1787 (2006).
- [85] J. Heyd, G. E. Scuseria, and M. Ernzerhof, Hybrid functionals based on a screened coulomb potential, *J. Chem. Phys.* **118**, 8207 (2003).
- [86] A. V. Krukau, O. A. Vydrov, A. F. Izmaylov, and G. E. Scuseria, Influence of the exchange screening parameter on the performance of screened hybrid functionals, *J. Chem. Phys.* **125**, 224106 (2006).
- [87] W. Tang, E. Sanville, and G. Henkelman, A grid-based bader analysis algorithm without lattice bias, *J. Phys.: Condens. Matter* **21**, 084204 (2009).
- [88] E. Sanville, S. D. Kenny, R. Smith, and G. Henkelman, Improved grid-based algorithm for bader charge allocation, *J. Comput. Chem.* **28**, 899 (2007).
- [89] G. Henkelman, A. Arnaldsson, and H. Jónsson, A fast and robust algorithm for bader decomposition of charge density, *Comput. Mater. Sci.* **36**, 354 (2006).
- [90] A. Togo and I. Tanaka, First principles phonon calculations in materials science, *Scripta Mater.* **108**, 1 (2015).

- [91] D. Pines and D. Bohm, A collective description of electron interactions: Ii. collective vs individual particle aspects of the interactions, *Phys. Rev.* **85**, 338 (1952).
- [92] M. Gajdoš, K. Hummer, G. Kresse, J. Furthmüller, and F. Bechstedt, Linear optical properties in the projector-augmented wave methodology, *Phys. Rev. B* **73**, 045112 (2006).
- [93] K. Ren, M. Sun, Y. Luo, S. Wang, J. Yu, and W. Tang, First-principle study of electronic and optical properties of two-dimensional materials-based heterostructures based on transition metal dichalcogenides and boron phosphide, *Appl. Surf. Sci.* **476**, 70 (2019).
- [94] X. Zhang, Y. Song, F. Zhang, Q. Fan, H. Jin, S. Chen, Y. Jin, S. Gao, Y. Xiao, and N. Mwanemwa *et al.*, The electronic properties of hydrogenated janus mosse monolayer: A first principles investigation, *Mater. Res. Express* **6**, 105055 (2019).
- [95] W.-J. Yin, B. Wen, G.-Z. Nie, X.-L. Wei, and L.-M. Liu, Tunable dipole and carrier mobility for a few layer janus mosse structure, *J. Mater. Chem. C* **6**, 1693 (2018).
- [96] J. Yuan, S. Najmaei, Z. Zhang, J. Zhang, S. Lei, P. M. Ajayan, B. I. Yakobson, and J. Lou, Photoluminescence quenching and charge transfer in artificial heterostacks of monolayer transition metal dichalcogenides and few-layer black phosphorus, *Acs Nano* **9**, 555 (2015).